

Faster VGGT with Block-Sparse Global Attention

Chung-Shien Brian Wang

Christian Schmidt

Jens Piekenbrinck

Bastian Leibe

Computer Vision Group
RWTH Aachen University

Abstract

Efficient and accurate feed-forward multi-view reconstruction has long been an important task in computer vision. Recent transformer-based models like VGGT and π^3 have achieved impressive results with simple architectures, yet they face an inherent runtime bottleneck, due to the quadratic complexity of the global attention layers, that limits the scalability to large image sets. In this paper, we empirically analyze the global attention matrix of these models and observe that probability mass concentrates on a small subset of patch-patch interactions that correspond to cross-view geometric matches. Motivated by the structured attention and inspired by recent advancement in large language models, we propose a replacement for the dense global attention operation based on highly optimized block-sparse kernels, yielding up to $4\times$ faster inference with comparable task performance. Our retrofit requires no retraining of the backbone, extends to both VGGT and π^3 , and supports large image collections. Evaluations on a comprehensive suite of multi-view benchmarks demonstrate the effectiveness of our approach.

1. Introduction

Reconstruction of 3D geometry and camera motion from multiple images is a central, long-standing problem in computer vision that has a broad impact across domains such as autonomous driving, embodied agents, AR/VR or photogrammetry. Classical pipelines approach this task using optimization-based explicit geometric modeling and iterative refinement, most notable bundle adjustment, yielding reliable results at the cost of significant runtime overhead [21, 24]. More recently, feed-forward models [18, 30, 35] have narrowed the gap to structure-from-motion (SfM) systems such as COLMAP [24]. A prevalent concept in this family of networks, originating with DUST3R [35], is to estimate 3D geometry and relative cameras from image-pairs and subsequently consolidate predictions across multiple views.

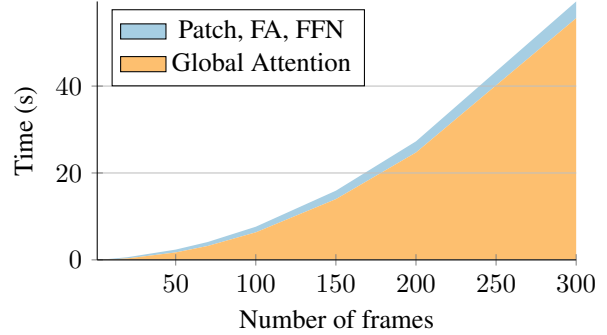


Figure 1. **Runtime of VGGT’s forward pass.** FA denotes frame-wise attention. As the number of input frames increases, global attention dominates the computational cost (measured with FlashAttention2 [7] on an H100 GPU at resolution 518^2). We propose to adapt a block-sparse attention method that considerably reduces the cost of Global Attention while preserving result quality.

The recently proposed *Visual Geometry Grounded Transformer (VGGT)* [33] is a particularly simple and effective model for multi-view geometry estimation model, achieving state-of-the-art performance on reconstruction, pointmap estimation and point tracking. A key architectural design element of VGGT is the use of global attention blocks in the decoder, which enables holistic, scene-level reasoning in a single forward pass. However, the complexity of global attention grows quadratically with the number of input images, thereby becoming the dominant computational contributor even at moderate sequence lengths, as illustrated in Fig. 1, and limiting scalability to larger image collections.

By inspecting the global attention maps during a forward pass of the model, visualized in Fig. 3, we observe that each token only attends to a small subset of tokens, leading to sparse attention matrices. This observation motivates our systematic analysis of these sparsity patterns, suggesting that a substantial portion of the computational complexity of the global attention layers can potentially be avoided without degrading task performance.

Building on these findings and inspired by recent ad-

vances in large language models [13], we propose a novel adaptive block-sparse attention mechanism that approximates the full attention map and computes attention using block-sparse kernels whose cost scales with the number of active blocks rather than the full quadratic size, ultimately accelerating inference. The additional module is lightweight and does not require any optimization, avoiding the need of extra annotations or backward passes through the original VGGT model. With extensive experiments across multiple datasets, we empirically demonstrate that our method achieves task performance on par with the original VGGT model, while substantially accelerating inference speed up to 400%.

To further showcase the versatility of our approach, we apply the sparse block-attention mechanism to the recent π^3 variant of VGGT that facilitates permutation-invariant geometry estimation [36] and observe similar accuracy-efficiency trade-offs.

Overall, our contributions are threefold: (1) an analysis of sparsity-patterns in global attention layers of multi-view geometry estimation transformer models; (2) a novel adaptive block-sparse attention mechanism to accelerate inference speed without requiring optimization; and (3) comprehensive empirical evaluations demonstrating matched accuracy with significantly reduced compute.

2. Related Work

2.1. Feed-Forward Multi-View Reconstruction

Traditional multi-view reconstruction pipelines follow the *Structure from Motion (SfM)* paradigm, jointly estimating scene geometry and camera poses [14, 21, 24, 25]. Typical implementations perform feature extraction and matching, triangulation, and bundle adjustment. An additional dense depth estimation stage is necessary if a dense reconstruction is desired. COLMAP [24] remains a widely adapted pipeline and is frequently employed as baseline or used to produce ground-truth annotations for datasets.

Learning-based approaches for multi-view reconstruction aim to enhance or replace these pipelines. A prominent line of work employs a cross-attention decoder to match two input frames [11, 15, 18, 35]. Scaling such methods to many views requires an additional global alignment post-processing step that consolidates pairwise predictions into a single, consistent scene representation [11, 18, 35]. But this consolidation is computationally expensive and introduces a separate source of error.

To mitigate the cost of globally aligning image-pairs, several derivative works incrementally extend the reconstruction [12, 32, 34] by iteratively applying two-view models. Some maintain a persistent latent representation to accumulate information [32, 34], while Light3r-SfM [12] directly updates a global reconstruction and shows improved

performance on large scenes. Despite their practicality, iterative schemes may not perform as well as methods that consider all views simultaneously. Incremental updates are order-sensitive, prone to error accumulation and drift, and require revisiting past states or additional optimization to enforce long-range, cross-view consistency. In contrast, globally conditioned models can exploit holistic context to align distant views and resolve ambiguities in a single forward pass, albeit at higher computational cost.

2.2. Global Attention for Fast 3D Processing

In contrast to two-view models, architectures with global attention mechanisms are able to reason jointly over all views at once, enabling scene-level consistency [3, 33, 36, 37]. Fast3r [37] combines a per-frame feature encoder with a decoder composed exclusively of global attention blocks, hence lacking frame-wise attention blocks. In addition, it predicts both local and global pointmaps for every view, a design inherited from two-view models.

VGGT [33] simplifies reconstruction by predicting all pointmaps in the coordinate system of a reference view, *i.e.* the first view. Its decoder alternates between frame-wise and global attention, allowing per-frame features to be adapted before the next round of global matching. For reference, we provide an overview of the VGGT architecture in Fig. 2.

Since VGGT predicts all pointmaps with respect to the reference view and employs camera embeddings, its predictions are sensitive to input ordering. To alleviate this issue, π^3 [36] removes the camera embeddings to attain permutation invariance while retaining per-frame register tokens akin to VGGT. The authors report slightly improved reconstruction quality over VGGT on most benchmarks, with notably reduced variance across input permutations.

Despite their architectural differences, these methods share a reliance on global attention, whose time complexity scales quadratically with the number of tokens, which motivates our approach to exploit the sparsity of global attention to preserve reconstruction performance while reducing computational overhead.

2.3. Sparse Attention

Attention is the foundation of many state-of-the-art neural architectures, especially large language models (LLMs). A growing area of research aims to reduce the quadratic complexity of dense attention by exploiting structure in the attention map [13, 39]. However, LLM-oriented techniques often rely on autoregressive assumptions, like causal masking and KV-caching during inference, that do not directly transfer to attention over continuous, 2D token grids as used in vision models.

A more generally applicable approach is block-sparse attention [4], which combines the hardware-friendly block-

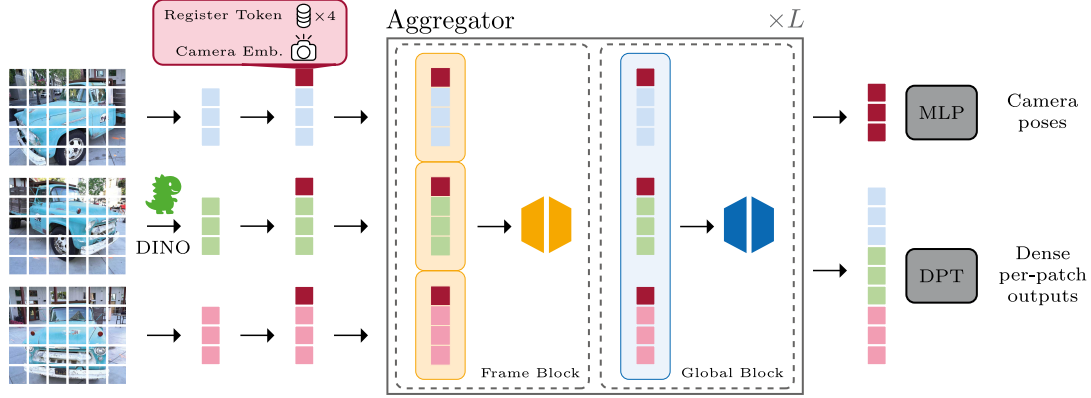


Figure 2. **Architecture overview of VGGT [33].** The key component is the Aggregator consisting of $L = 24$ alternating attention blocks (first frame-wise attention, then global attention over all frames). Each input frame is augmented with five learned embedding vectors: one camera token and four register tokens. After the Aggregator, VGGT regresses camera poses from the camera tokens using a light-weight MLP head, and dense outputs (point maps, depth, point tracks) using DPT heads [22].

wise computation of Flash Attention with a sparse block mask. Building on this paradigm, SparseAttention [39] recently demonstrated the practicality of block-sparse attention across diverse models and modalities. In this work, we adopt SparseAttention to accelerate the inference of VGGT and π^3 , showing speed-ups of up to $4\times$ while preserving the task performances of these models. While [39] reported results up to 128K tokens with 54% sparsity under causal attention, our largest configuration processes sequences exceeding 512K tokens, at a sparsity ratio of over 75%.

3. Analyzing VGGT’s Attention Patterns

Traditional multi-view reconstruction pipelines rely heavily on hand-crafted features, *e.g.* SIFT [19], in order to establish sparse correspondences that drive structure and camera estimation [24, 25]. Our analysis of the global attention maps in VGGT reveals a strong concentration on a limited set of token pairs, resulting in sparse patterns that are analogous to correspondence matrices and that mirror geometric matching. The key idea of our approach is to exploit these sparsity patterns to improve the efficiency of global attention.

3.1. Background: VGGT’s Architecture

An overview of the VGGT architecture is illustrated in Fig. 2. We briefly recapitulate the most important parts of the architecture for completeness.

VGGT consists of a patchifier P , a feature aggregator A , and several task-specific heads H_1, \dots, H_T . The patchifier P independently transforms each input image I into a set of patch tokens $T = P(I)$. VGGT employs a pre-trained DINOv2-Large [20] with a patch size of 14×14 pixels [33].

For every frame, VGGT concatenates five special tokens to the patch tokens: a camera token that allows the model to differentiate frames, and four register tokens [9]. Furthermore, VGGT maintains one set of special tokens for the first frame and another set for all other frames, which allows the model to distinguish between the reference view and other auxiliary frames. The aggregator A is a series of transformer blocks alternating between global and frame-wise attention. Global attention computes full self-attention over the union of all patch and special tokens across all frames, which enables scene-level reasoning. Frame-wise attention performs self-attention between the patch and special tokens of a single frame, which supports per-frame adaptation. Both frame-wise and global attention layers are followed by two-layer per-token MLPs, as it is common in transformer architectures [10]. After the final aggregator layer, the register tokens are discarded and the remaining tokens are passed to the task-specific heads. VGGT employs a lightweight head for pose regression and DPT [22] heads for dense prediction tasks such as depth and pointmaps. Our analysis focuses on the global attention layers inside the aggregator.

The follow-up model π^3 [36] closely matches VGGT’s architecture with just a few modifications to promote permutation invariance. Architecturally, π^3 uses fewer alternating attention blocks in the aggregator, 18 instead of 24, replaces DPT with plain Transformer heads for dense prediction tasks and removes camera embeddings while retaining per-frame register tokens. Methodologically, π^3 supervises relative poses between all frames rather than coordinates tied to the reference view. The authors show that these modifications improve the models task performance and reduce sensitivity to input permutations [36].

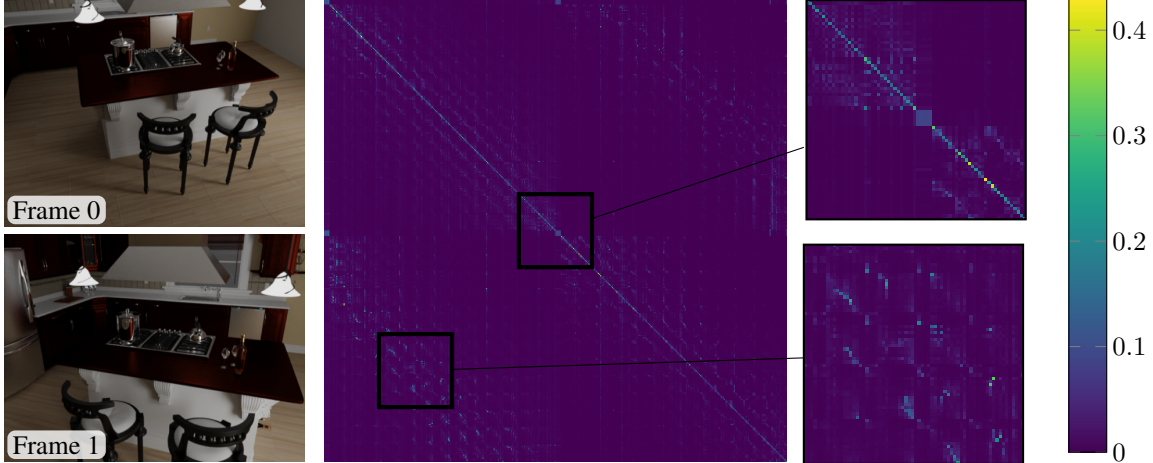


Figure 3. **Visualization of VGGT’s global attention matrix.** A very small number of entries is highly activated, while the vast majority of entries is near zero. This visualization shows the average attention map over all heads of layer 15 in the VGGT aggregator, at an input resolution of 224×182 . Upper highlight: The special tokens attend to each other and form a distinctive pattern. Lower highlight: Patch-level attention is localized on a small subset of highly activated entries. See the supplementary material for an enlarged visualization.

3.2. Visualizing Attention Maps

We visualize the full post-softmax attention map for a representative global attention block in a middle decoder layer, layer 15, in Fig. 3. Only a small fraction of entries carry non-negligible probability mass, indicating pronounced sparsity. To study how this behavior evolves with layer depth, Fig. 4 (right) plots the average and the maximum activation of different parts of the attention map against the layer index. We observe a peak in the maximum activation values in the middle of the aggregator. This effect is concentrated in patch-patch interactions, whereas attention involving special tokens remains stable across layers. The sparse, highly activated entries align with geometrically meaningful correspondences between frames, as illustrated in Fig. 4 (left).

We hypothesize that the model learns to perform an exhaustive correspondence search over the layers of the aggregator. More concretely, the global attention proposes cross-view correspondences and exchanges information across frames, while the frame-wise attention adapts the features of the patch tokens to allow the model to find better matches in the subsequent global layers. The plots in Fig. 4 (right) show that the mid-aggregator layers exhibit the strongest selective attention and appear to contribute disproportionately to multi-view reasoning.

3.3. Are Some Layers More Important?

To further test our hypothesis that the mid-layers of the aggregator are most important for task performance, we conduct a layer-drop ablation in which selected aggregator blocks are skipped at inference. We show the ablation results in Fig. 5 and show additional results in the supplemen-

tary material.

The model is comparatively robust when early or late aggregator layers are skipped. In contrast, omitting a single middle layer leads to a pronounced performance drop. This behaviour supports our hypothesis that the middle of the aggregator concentrates the essential cross-view information exchange and motivates our adaptive block-selection strategy.

3.4. Consequences of this Analysis

Our analysis yields three take-away messages. First, global attention is highly sparse. Second, the variation in attention entries is dominated by patch–patch interactions, while special token interactions remain stable across depth. Lastly, mid-stack layers carry the key cross-view integration, as confirmed by the layer-drop ablation. These findings indicate that dense quadratic attention is not necessary throughout the stack, but that considerable efficiency gains can be realized by exploiting sparsity, in particular in the important middle layers.

Guided by this analysis, we propose to replace the dense global attention layers with an adaptive block-sparse variant. This reduces the time complexity with minimal accuracy loss and integrates into VGGT and π^3 without changes to their encoders or task heads.

4. Method

In this section, we describe our baseline method for block-sparse attention in the global attention layer in VGGT (Sec. 4.1) and how we adapt it to handle camera and register tokens (Sec. 4.2). Note that while we utilize the implementation of SparseAttention [39], block-sparse attention in it-

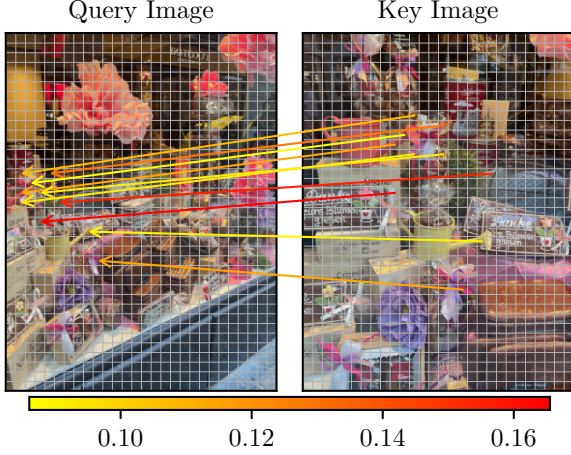


Figure 4. **VGGT’s global attention matrix is extremely sparse.** Left: We visualize the tokens corresponding to the top-k activated entries of the attention map of layer 15. Right: Average & maximum attention scores in the global attention maps; the shorthand {S,P}2{P,S} denotes attention between special (S) and patch (P) tokens. Layers in the middle of the aggregator exhibit higher activations and increased sparsity. Note the different scalings of the mean and max activations.

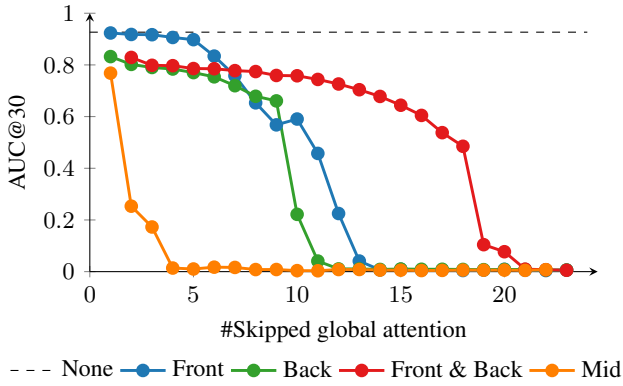


Figure 5. **Influence of dropping global attention layers.** We skip the computation of different global attention layers in the aggregator starting with the earliest (Front), last (Back), alternating (Front & Back), or from the middle layers (Middle), and evaluate pose estimation on CO3Dv2 [23]. The x-axis denotes the total number of skipped layers. The experiment shows that the model is especially sensitive to pruning of the center layers, and robust against pruning the early and late layers.

self is independent of this particular work and could, for example, be implemented on top of Flash Attention [7, 8, 40] to yield similar results.

4.1. Block-Sparse Attention

Self-Attention. Self-Attention is the cornerstone of many modern neural networks, as it enables dynamic, global interactions between input elements. Given $\mathbf{X} \in \mathbb{R}^{n \times d}$, queries, keys, and values are computed as $\mathbf{Q} = \mathbf{XW}^Q$,

$\mathbf{K} = \mathbf{XW}^K$, $\mathbf{V} = \mathbf{XW}^V$, and the scaled dot-product attention is defined as

$$\text{Attention}(\mathbf{Q}, \mathbf{K}, \mathbf{V}) = \text{softmax}\left(\frac{\mathbf{QK}^\top}{\sqrt{d_h}}\right) \mathbf{V}. \quad (1)$$

Multi-head attention concatenates H such projections to enhance expressivity [31]. For long input sequences, computing the full attention matrix $\mathbf{A} = \mathbf{QK}^\top$ is the bottleneck of the operation. For a moderate input length of 10 frames at resolution 518^2 , the global attention matrix would already contain $(10 \cdot \frac{518^2}{14})^2 \approx 1.8 \cdot 10^8$ elements, whereas for 100 frames, the attention matrix would take around 35GB at half precision.

Block-Sparse Attention. Sparse attention reduces the quadratic cost of full attention by constraining the pattern of non-zero entries in \mathbf{QK}^\top . Instead of attending to all positions, only predefined entries are computed:

$$\text{SparseAttn}(\mathbf{Q}, \mathbf{K}, \mathbf{V}) = \text{softmax}\left(\frac{(\mathbf{QK}^\top) \odot \mathbf{M}}{\sqrt{d_h}}\right) \mathbf{V}, \quad (2)$$

where \mathbf{M} is a binary sparsity mask and the \odot operator denotes the element-wise (Hadamard) product. In practice, block-sparse masks are preferred, as they align with modern hardware accelerators, enabling efficient memory access and parallelization [2, 5, 8].

Predicting Block Masks. To predict the importance of blocks from queries and keys, we first apply average pooling with block size b to the queries \mathbf{Q} and keys \mathbf{K} , yielding pooled representations $P^b(\mathbf{Q})$ and $P^b(\mathbf{K})$. We then compute their similarity matrix $\mathbf{S} = P^b(\mathbf{Q})P^b(\mathbf{K})^\top$ and apply a softmax to obtain probability distributions over blocks.

The resulting distribution provide a natural way for ranking candidate blocks, from which we derive a binary block-sparsity mask using either top- k style selection and cumulative density function (CDF) thresholding. The mask directly determines which query-key blocks are evaluated, and can be used directly with standard block-sparse attention kernels. A graphical overview is provided in Fig. 6. We experiment with an additional linear projection layer after pooling queries and keys, but find no improvement over the baseline.

Selecting Blocks. We select blocks using two complementary criteria: a CDF threshold τ and a sparse ratio ρ . The CDF threshold ensures the selected set covers at least a τ fraction of predicted cumulative probability. The sparse ratio acts as a lower bound, enforcing a minimum of $k = \lfloor B \cdot (1 - \rho) \rfloor$ top-ranked blocks, where B denotes the total number of blocks. The two criteria complement each other: In uniform layers, a fixed sparse ratio alone may admit too few blocks, while the CDF threshold guarantees sufficient coverage; in sparse layers, the threshold may be met with very few blocks, while the sparse ratio ensures that at least a reasonable minimum is preserved. Together, they adapt block selection to diverse sparsity patterns while maintaining stability and efficiency.

Comparison to SpargeAttention. While our method is related to SpargeAttention [39], the approaches differ in design and implementation trade-offs. SpargeAttention introduces additional mechanisms such as self-similarity filtering and warp-level PV pruning, which increases implementation complexity and maintenance overhead across GPU generations. In contrast, our method is kernel-agnostic. It produces a binary block mask from pooled query-key similarities, and blocks are chosen based on a fixed sparse ratio and a CDF threshold, hence compatible with any standard block-sparse attention kernel. This decoupling from hardware-specific optimizations makes our approach simpler to implement, easier to maintain, and more robust to future accelerator iterations.

4.2. Handling Special Tokens

VGGT employs register tokens [9] in addition to learned camera tokens which differentiate between frames. We find that these tokens behave qualitatively differently from the regular patch tokens, and pooling them together results in worse performance for similar sparsity ratios. We therefore split the tokens into two sets: \mathbf{X}_p containing the patch tokens, and \mathbf{X}_s , containing the special tokens, *i.e.* register and camera tokens. We only predict and use the block sparse map on the patch tokens \mathbf{X}_p , and compute the full attention on \mathbf{X}_s , as well as cross-attention between \mathbf{X}_s and \mathbf{X}_p and vice-versa. We find that this strategy is essential to avoid large drops in task performance.

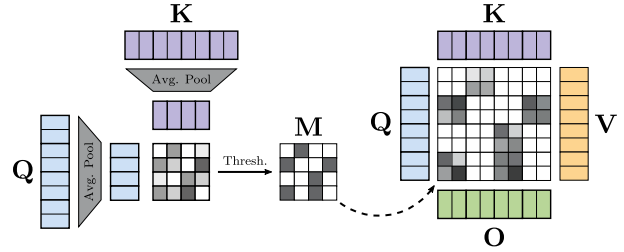


Figure 6. **Overview of the training-free adaptive sparse attention.** Keys and queries are average pooled to estimate a low-resolution approximation of the attention map. This low-resolution attention map is used to create the binary mask for block-sparse attention.

5. Experiments

We extend two large reconstruction models, VGGT [33] and π^3 [36], with the described sparse global attention mechanism and evaluate the performance impact on common multi-view benchmarks. In particular, we evaluate the robustness of the models against varying *sparsity ratios*, which we define as the ratio of computed entries of the attention map to the total number of entries. As the number of input frames increases, the theoretical speed-up from a sparsity ratio of x approaches $\frac{1}{1-x}$, since the overall computational costs are dominated by the global attention. Processing a 200 frame sequence with sparsity ratio of 0.75, for example, will accelerate the global attention by a factor of four. Depending on the ratio of global attention to the overall runtime, the end-to-end speed-up will be lower.

In the main text, we show results for commonly used benchmarks on relative pose estimation (Real Estate 10K [41], Common Objects in 3D [23] TUM [29], and ScanNet [6]), and pointmap estimation (7Scenes [28], NRGBD [1], DTU [16], and ETH3D [26]). Additionally, we show results for scene-level pose estimation on the Tanks & Temples dataset [17].

5.1. Regression Tests

We evaluate our sparsified model on relative pose and pointmap estimation, using a range of common benchmark datasets. Unless indicated otherwise, we closely follow the setting of the original VGGT paper [33]. For a comprehensive high-level overview of the results, we visualize the sparsity-performance trade-off in Fig. 7. The results show that task performance degrades comparatively little with increasing sparsity. Both VGGT and π^3 achieve results comparable to other state-of-the-art models even at high sparsity ratios, which is further corroborated by the qualitative examples provided in Fig. 8.

Pose Estimation asks to predict the 6DoF pose of all

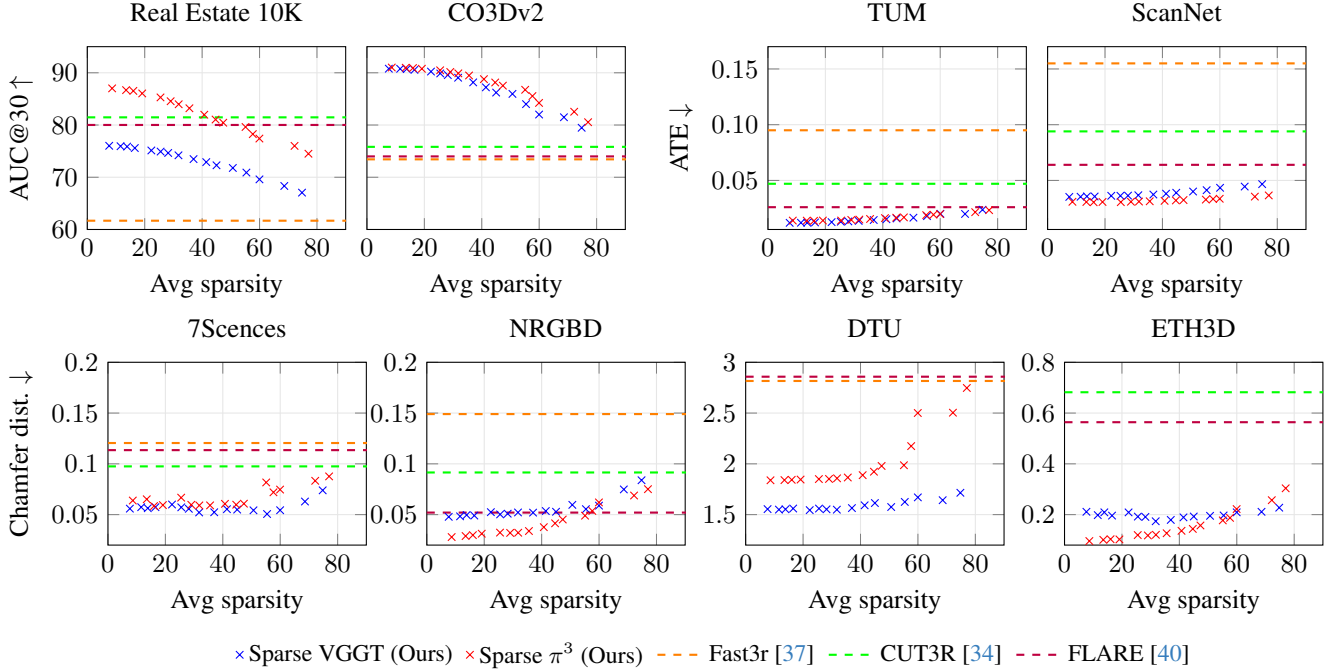


Figure 7. **Results for Relative Pose Estimation (top) Multi-View Reconstruction (bottom).** Multi-view reconstruction performance seems to be robust against sparsification of global attention; even in the highest sparsity settings, the results are on par or better than other state-of-the-art methods. We provide comprehensive tables for these results in the supplementary material.

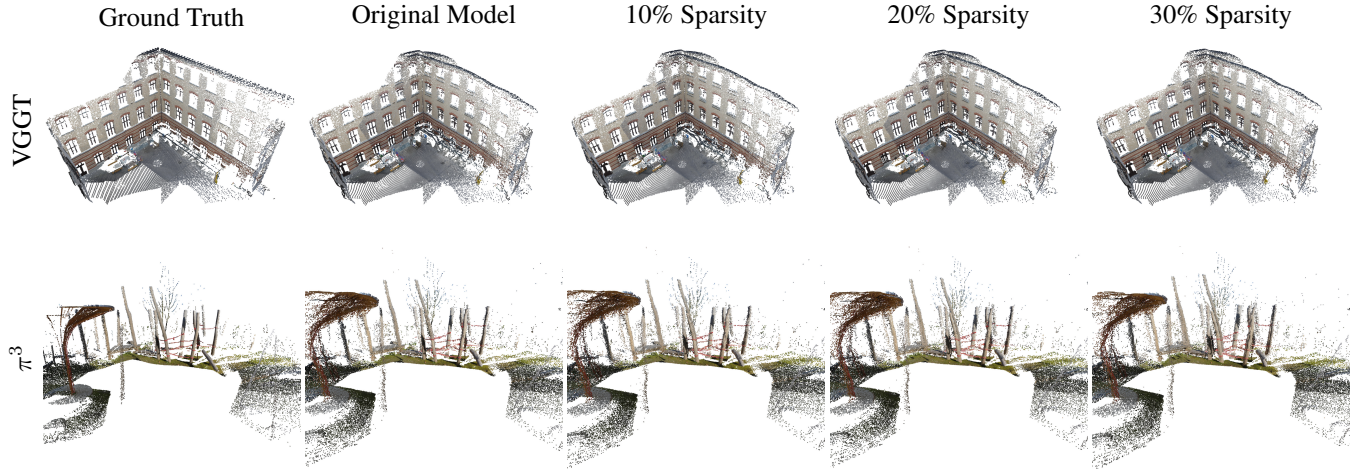


Figure 8. **Qualitative examples.** We show examples from the ETH3D dataset [26]. Increasing sparsity leads to small perturbations in the reconstruction, but the overall quality stays remarkably high.

input views. We run evaluation on Common Objects in 3D [23] and Real Estate 10K [41]. We show aggregate results in Fig. 7 (top). While we observe a continuous decrease in pose accuracy for increasing sparsity levels, the modified model still performs on par with or even better than other state-of-the-art methods.

Multi-view Pointmap Estimation is the task of predicting the surface 3D point for each pixel in all input images. We evaluate on ETH3D [26] and DTU [16], using ten random frames per scene for a fair comparison with VGGT [33]. We show a compact representation of the results in Fig. 7 and full result tables in the supplementary. We observe a

	Method	RRA@5↑	RTA@5↑	ATE↓	Time [s]↓
25	VGGT	84.4	81.5	0.033	0.63
	VGGT-S25	83.8	80.6	0.032	0.66
	VGGT-S50	81.4	79.5	0.032	0.56
	VGGT-S75	56.9	65.6	0.037	0.54
	π^3	84.4	83.8	0.020	0.62
	π^3 -S25	84.4	83.5	0.020	0.66
	π^3 -S50	82.6	82.1	0.019	0.64
	π^3 -S75	56.9	65.6	0.025	0.65
50	VGGT	84.8	81.5	0.023	1.5
	VGGT-S25	83.8	80.9	0.023	1.2
	VGGT-S50	81.6	79.5	0.023	1.1
	VGGT-S75	57.3	61.0	0.025	1.0
	π^3	85.4	84.6	0.015	2.1
	π^3 -S25	84.5	83.9	0.015	1.2
	π^3 -S50	82.3	82.9	0.015	1.1
	π^3 -S75	57.9	67.0	0.016	1.0
100	VGGT	84.8	81.3	0.015	7.9
	VGGT-S25	83.9	80.8	0.016	2.9
	VGGT-S50	81.7	79.7	0.016	2.6
	VGGT-S75	58.1	61.5	0.017	2.1
	π^3	85.7	84.6	0.012	4.3
	π^3 -S25	84.9	84.2	0.012	2.5
	π^3 -S50	83.0	83.0	0.012	2.2
	π^3 -S75	58.9	67.2	0.012	1.8
200	VGGT	83.9	79.9	0.012	18
	VGGT-S25	83.1	79.6	0.011	8.5
	VGGT-S50	80.7	78.4	0.011	7.3
	VGGT-S75	57.1	60.8	0.013	5.5
	π^3	85.4	83.9	0.009	13.9
	π^3 -S25	84.6	83.5	0.009	6.8
	π^3 -S50	82.9	82.3	0.009	5.8
	π^3 -S75	59.8	67.7	0.009	4.4
full	VGGT	73.4	72.5	0.008	35
	VGGT-S25	72.7	72.2	0.009	17.9
	VGGT-S50	70.3	71.1	0.008	14.4
	VGGT-S75	46.0	53.0	0.009	10.4
	π^3	75.8	75.8	0.006	27.9
	π^3 -S25	74.8	75.3	0.006	13.6
	π^3 -S50	73.0	74.2	0.006	11.3
	π^3 -S75	50.0	59.1	0.006	7.8

Table 1. **Feed-Forward Camera Pose Estimation on Tanks & Temples [17]**. Timings were recorded on an NVIDIA H100 at a resolution of 294×518 .

similar trend as before, with high sparsity ratios performing continuously well.

5.2. Scene-Level Relative Pose Estimation

In order to test the scalability of VGGT and the generalization of the linear sparsity predictors, we evaluate pose estimation on the Tanks & Temples benchmark [17], following the setup of previous works [11, 12]. We present the results in Fig. 9 and Tab. 1.

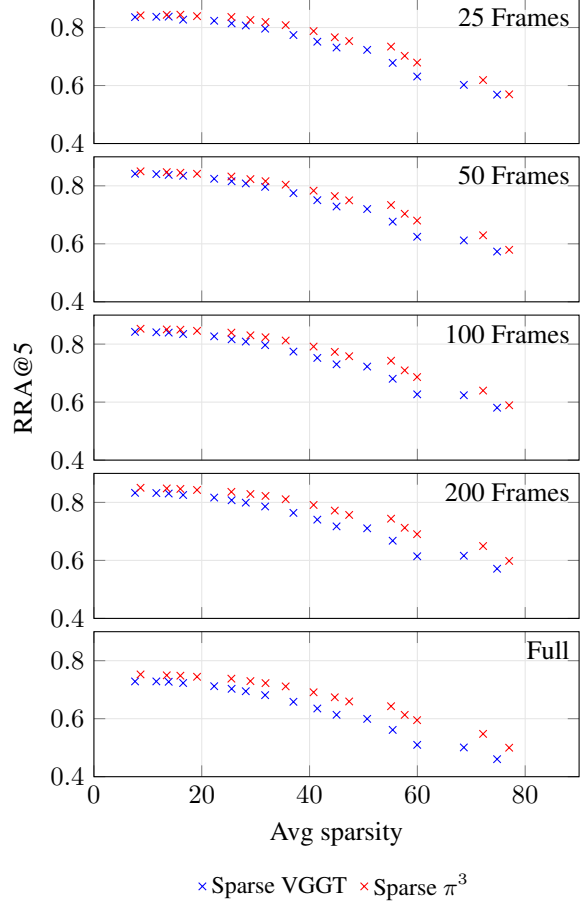


Figure 9. **Results on Tanks & Temples for different input sizes and sparsity ratios.**

6. Discussion

We analyzed global attention in transformer-based geometry estimators, VGGT and π^3 , and found that it exhibits unstructured sparsity patterns, which can be interpreted as exhaustive correspondence search, and is most pronounced in the middle aggregator layers. Building on these observations, we adapted a block-sparse global attention mechanism for patch-patch interactions, improving scalability to large image sets. Our approach achieves task performance comparable to the original model while being up to four times faster during inference on large-scale scenes.

While we focused on increasing the number of input images in this study, our approach is also applicable to speed up inference on higher-resolution inputs. Doubling the input resolution results in four times as many patch tokens and in turn to $16\times$ more compute spent on global attention, drastically exacerbating the existing bottleneck.

Exploiting block-wise sparsity is orthogonal to other acceleration approaches like FlashAttention [7, 8, 27], and can

potentially be integrated into the training procedure to reduce the impact on task performance.

Acknowledgments. Christian Schmidt is funded by BMBF project bridgingAI (16DHBKI023). Jens Pickenbrinck’s research is funded by the Bosch-RWTH LHC project ”Context Understanding for Autonomous Systems”. Computations were performed with computing resources granted by RWTH Aachen University under projects `thes2009` and `rwth1849`. The authors thank Karim Abou Zeid and Kadir Yilmaz for helpful feedback and Laura Schneider for help with visualizations.

References

- [1] Dejan Azinović, Ricardo Martin-Brualla, Dan B Goldman, Matthias Nießner, and Justus Thies. Neural rgb-d surface reconstruction. In *CVPR*, 2022. 6, 11
- [2] Iz Beltagy, Matthew E Peters, and Arman Cohan. Longformer: The long-document transformer. *arXiv preprint arXiv:2004.05150*, 2020. 5
- [3] Yohann Cabon, Lucas Stofl, Leonid Antsfeld, Gabriela Csurka, Boris Chidlovskii, Jerome Revaud, and Vincent Leroy. Must3r: Multi-view network for stereo 3d reconstruction. In *CVPR*, 2025. 2
- [4] Beidi Chen, Tri Dao, Kaizhao Liang, Jiaming Yang, Zhao Song, Atri Rudra, and Christopher Re. Pixelated butterfly: Simple and efficient sparse training for neural network models. In *ICLR*, 2022. 2
- [5] Rewon Child, Scott Gray, Alec Radford, and Ilya Sutskever. Generating long sequences with sparse transformers. *arXiv preprint arXiv:1904.10509*, 2019. 5
- [6] Angela Dai, Angel X Chang, Manolis Savva, Maciej Halber, Thomas Funkhouser, and Matthias Nießner. Scannet: Richly-annotated 3d reconstructions of indoor scenes. In *Proceedings of the IEEE conference on computer vision and pattern recognition*, pages 5828–5839, 2017. 6, 13
- [7] Tri Dao. Flashattention-2: Faster attention with better parallelism and work partitioning. *arXiv preprint arXiv:2307.08691*, 2023. 1, 5, 8
- [8] Tri Dao, Dan Fu, Stefano Ermon, Atri Rudra, and Christopher Ré. Flashattention: Fast and memory-efficient exact attention with io-awareness. *NeurIPS*, 2022. 5, 8
- [9] Timothée Darcet, Maxime Oquab, Julien Mairal, and Piotr Bojanowski. Vision transformers need registers, 2023. 3, 6
- [10] Alexey Dosovitskiy, Lucas Beyer, Alexander Kolesnikov, Dirk Weissenborn, Xiaohua Zhai, Thomas Unterthiner, Mostafa Dehghani, Matthias Minderer, G Heigold, S Gelly, et al. An image is worth 16x16 words: Transformers for image recognition at scale. In *ICLR*, 2020. 3
- [11] Bardienus Duisterhof, Lojze Züst, Philippe Weinzaepfel, Vincent Leroy, Yohann Cabon, and Jerome Revaud. Mast3r-sfm: a fully-integrated solution for unconstrained structure-from-motion. *arXiv preprint arXiv:2409.19152*, 2024. 2, 8
- [12] Sven Elflein, Qunjie Zhou, and Laura Leal-Taixé. Light3r-sfm: Towards feed-forward structure-from-motion. In *CVPR*, 2025. 2, 8
- [13] Yizhao Gao, Zhichen Zeng, Dayou Du, Shijie Cao, Peiyuan Zhou, Jiaxing Qi, Junjie Lai, Hayden Kwok-Hay So, Ting Cao, Fan Yang, et al. Seerattention: Learning intrinsic sparse attention in your llms. *arXiv preprint arXiv:2410.13276*, 2024. 2, 1
- [14] Richard Hartley and Andrew Zisserman. *Multiple view geometry in computer vision*. Cambridge university press, 2003. 2
- [15] Wonbong Jang, Philippe Weinzaepfel, Vincent Leroy, Lourdes Agapito, and Jerome Revaud. Pow3r: Empowering unconstrained 3d reconstruction with camera and scene priors. In *CVPR*, 2025. 2
- [16] Rasmus Jensen, Anders Dahl, George Vogiatzis, Engil Tola, and Henrik Aanæs. Large scale multi-view stereopsis evaluation. In *CVPR*, 2014. 6, 7, 9
- [17] Arno Knapitsch, Jaesik Park, Qian-Yi Zhou, and Vladlen Koltun. Tanks and temples: Benchmarking large-scale scene reconstruction. *ACM TOG*, 2017. 6, 8, 15, 16, 17, 18, 19
- [18] Vincent Leroy, Yohann Cabon, and Jérôme Revaud. Grounding image matching in 3d with mast3r. In *ECCV*, 2024. 1, 2
- [19] David G Lowe. Distinctive image features from scale-invariant keypoints. *IJCV*, 2004. 3
- [20] Maxime Oquab, Timothée Darcet, Théo Moutakanni, Huy Vo, Marc Szafraniec, Vasil Khalidov, Pierre Fernandez, Daniel Haziza, Francisco Massa, Alaaeldin El-Nouby, et al. Dinov2: Learning robust visual features without supervision. *arXiv preprint arXiv:2304.07193*, 2023. 3
- [21] Linfei Pan, Dániel Baráth, Marc Pollefeys, and Johannes L Schönberger. Global structure-from-motion revisited. In *ECCV*, 2024. 1, 2
- [22] René Ranftl, Alexey Bochkovskiy, and Vladlen Koltun. Vision transformers for dense prediction. In *CVPR*, 2021. 3
- [23] Jeremy Reizenstein, Roman Shapovalov, Philipp Henzler, Luca Sbordone, Patrick Labatut, and David Novotny. Common objects in 3d: Large-scale learning and evaluation of real-life 3d category reconstruction. In *ICCV*, 2021. 5, 6, 7, 3, 8
- [24] Johannes Lutz Schönberger and Jan-Michael Frahm. Structure-from-motion revisited. In *CVPR*, 2016. 1, 2, 3
- [25] Johannes Lutz Schönberger, Enliang Zheng, Marc Pollefeys, and Jan-Michael Frahm. Pixelwise view selection for unstructured multi-view stereo. In *ECCV*, 2016. 2, 3
- [26] Thomas Schöps, Johannes L. Schönberger, Silvano Galliani, Torsten Sattler, Konrad Schindler, Marc Pollefeys, and Andreas Geiger. A multi-view stereo benchmark with high-resolution images and multi-camera videos. In *CVPR*, 2017. 6, 7, 10
- [27] Jay Shah, Ganesh Bikshandi, Ying Zhang, Vijay Thakkar, Pradeep Ramani, and Tri Dao. Flashattention-3: Fast and accurate attention with asynchrony and low-precision. *NeurIPS*, 2024. 8
- [28] Jamie Shotton, Ben Glocker, Christopher Zach, Shahram Izadi, Antonio Criminisi, and Andrew Fitzgibbon. Scene coordinate regression forests for camera relocalization in rgb-d images. In *CVPR*, 2013. 6, 7

- [29] Jürgen Sturm, Nikolas Engelhard, Felix Endres, Wolfram Burgard, and Daniel Cremers. A benchmark for the evaluation of rgb-d slam systems. In *2012 IEEE/RSJ international conference on intelligent robots and systems*, pages 573–580. IEEE, 2012. 6, 14
- [30] Zhenggang Tang, Yuchen Fan, Dilin Wang, Hongyu Xu, Rakesh Ranjan, Alexander Schwing, and Zhicheng Yan. Mv-dust3r+: Single-stage scene reconstruction from sparse views in 2 seconds. In *CVPR*, 2025. 1
- [31] Ashish Vaswani, Noam Shazeer, Niki Parmar, Jakob Uszkoreit, Llion Jones, Aidan N Gomez, Łukasz Kaiser, and Illia Polosukhin. Attention is all you need. *NeurIPS*, 2017. 5
- [32] Hengyi Wang and Lourdes Agapito. 3d reconstruction with spatial memory. In *3DV*, 2024. 2
- [33] Jianyuan Wang, Minghao Chen, Nikita Karaev, Andrea Vedaldi, Christian Rupprecht, and David Novotny. Vggg: Visual geometry grounded transformer. In *CVPR*, 2025. 1, 2, 3, 6, 7
- [34] Qianqian Wang, Yifei Zhang, Aleksander Holynski, Alexei A Efros, and Angjoo Kanazawa. Continuous 3d perception model with persistent state. In *CVPR*, 2025. 2, 7
- [35] Shuzhe Wang, Vincent Leroy, Yohann Cabon, Boris Chidlovskii, and Jerome Revaud. Dust3r: Geometric 3d vision made easy. In *CVPR*, 2024. 1, 2
- [36] Yifan Wang, Jianjun Zhou, Haoyi Zhu, Wenzheng Chang, Yang Zhou, Zizun Li, Junyi Chen, Jiangmiao Pang, Chunhua Shen, and Tong He. π^3 : Scalable permutation-equivariant visual geometry learning. *arXiv preprint arXiv:2507.13347*, 2025. 2, 3, 6
- [37] Jianing Yang, Alexander Sax, Kevin J Liang, Mikael Henaff, Hao Tang, Ang Cao, Joyce Chai, Franziska Meier, and Matt Feiszli. Fast3r: Towards 3d reconstruction of 1000+ images in one forward pass. In *CVPR*, 2025. 2, 7
- [38] Yao Yao, Zixin Luo, Shiwei Li, Jingyang Zhang, Yufan Ren, Lei Zhou, Tian Fang, and Long Quan. Blendedmvs: A large-scale dataset for generalized multi-view stereo networks. In *CVPR*, 2020. 1
- [39] Jintao Zhang, Chendong Xiang, Haofeng Huang, Haocheng Xi, Jun Zhu, Jianfei Chen, et al. Spargeattention: Accurate and training-free sparse attention accelerating any model inference. In *ICML*, 2025. 2, 3, 4, 6
- [40] Shangzhan Zhang, Jianyuan Wang, Yinghao Xu, Nan Xue, Christian Rupprecht, Xiaowei Zhou, Yujun Shen, and Gordon Wetzstein. Flare: Feed-forward geometry, appearance and camera estimation from uncalibrated sparse views. In *CVPR*, 2025. 5, 7
- [41] Tinghui Zhou, Richard Tucker, John Flynn, Graham Fyffe, and Noah Snavely. Stereo magnification: learning view synthesis using multiplane images. *ACM TOG*, 2018. 6, 7, 12

Faster VGGT with Block-Sparse Global Attention

Supplementary Material

A. Ablations

We present the results for two ablations of our method. In the first ablation, we evaluate whether it is necessary to distinguish between patch tokens and special tokens. In the second ablation, we investigate whether training linear projections on top of the pooled queries and keys improves the robustness of the method to sparsity.

A.1. Treating the special tokens special

In the main text, we distinguish between the special tokens, camera embedding and register tokens, and the patch tokens. We apply the block-sparse attention only on the patch-to-patch attention, while we compute the special-to-patch, patch-to-special, and the special-to-special attention as usual, *i.e.* dense. In this experiment, we compare this approach with an implementation that does not distinguish between the camera embeddings, register tokens, and patch tokens. The results are shown in Fig. A-1. At low sparsity levels, the chance of skipping computations concerning special tokens is small, since there are far more patch tokens than special tokens, and both methods perform similarly. At high sparsity levels, however, our strategy of always keeping all interactions concerning the camera and register tokens significantly reduces the performance degradation compared to the naive strategy.

A.2. Learning additional linear projections

We train additional linear projection layers on top of the pooled key and query representations following SeerAttention [13]. At training time, the linear projections are optimized to predict the entries of the downsampled attention map; at inference time, the predicted low-res attention map is converted into a binary block mask, as in the main text. With this experiment, we investigate whether the linear projections improve the robustness of the model for higher sparsity ratios compared to the default key and query representations.

Our training setup follows SeerAttention [13], that is, one linear projection per attention head. The training objective is a self-supervised KL loss between the downsampled ground-truth attention matrix and the logits of the predicted low-res mask. We train on BlendedMVS [38] because it contains real indoor and outdoor scenes and is similar to VGGT’s training data. Since no gradients need to be passed through the actual model, training is both fast and lightweight. We train the projection layers for 3k steps with a batch size of 16, and a sequence length of 8 frames at resolutions sampled from 518^2 and 518×378 , using the AdamW optimizer with a learning rate of 10^{-3} and weight decay of 0.01. The block size is set to 128 for the queries and 64 for the keys. Training finishes in around three hours on a single H100.

The results shown in Fig. A-2 show little to no improvements over the training-free baseline.

A.3. Full Layer Skip Ablations

We investigate the impact of skipping the global attention in the style of Fig. 5 in the main text on several other tasks. The results, shown in Fig. A-3, indicate a strong sensitivity of the model to perturbations in the middle layers, regardless of the task.

B. Additional Visualizations

B.1. π^3 attention maps are similar to VGGT’s

We plot the average and maximum value of the global attention matrix for layers in the aggregator of π^3 in Fig. A-4, in the same style as Fig. 4 in the main text. π^3 uses less global attention layers in the aggregator than VGGT, but the statistics of the remaining layers closely resemble those of the corresponding layers in VGGT.

B.2. High-res Attention Maps

We provide further visualizations of VGGT’s attention maps in Fig. A-5. Note that all attention map visualizations in this paper are done with inputs rescaled to at most 224px for better visibility of token activations.

B.3. Further Correspondence Visualizations

We provide additional qualitative results for correspondence estimation in Fig. A-6, demonstrating how VGGT and π^3 establish matches even in challenging scenarios with repeated structures and significant viewpoint changes.

C. Full Results Tables

For completeness, we provide the full results for all models in Fig. 7 and Fig. 9 in the tables on the following pages.

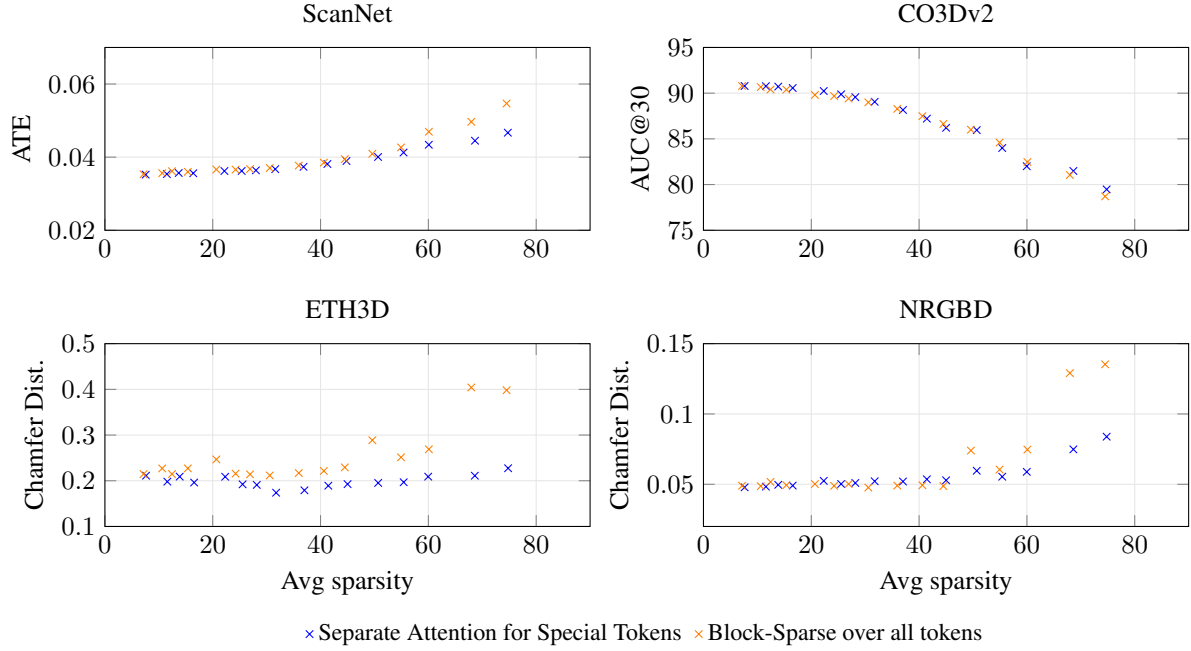


Figure A-1. **Ablation on special treatment of special tokens.** We compare the downstream performance of simple block-sparse attention over all tokens against our approach of separating patch tokens from camera and register tokens. For higher sparsity ratios, the chance of dropping special tokens rises, and at the same time, the task performance drops significantly more sharply for the simplified variant.

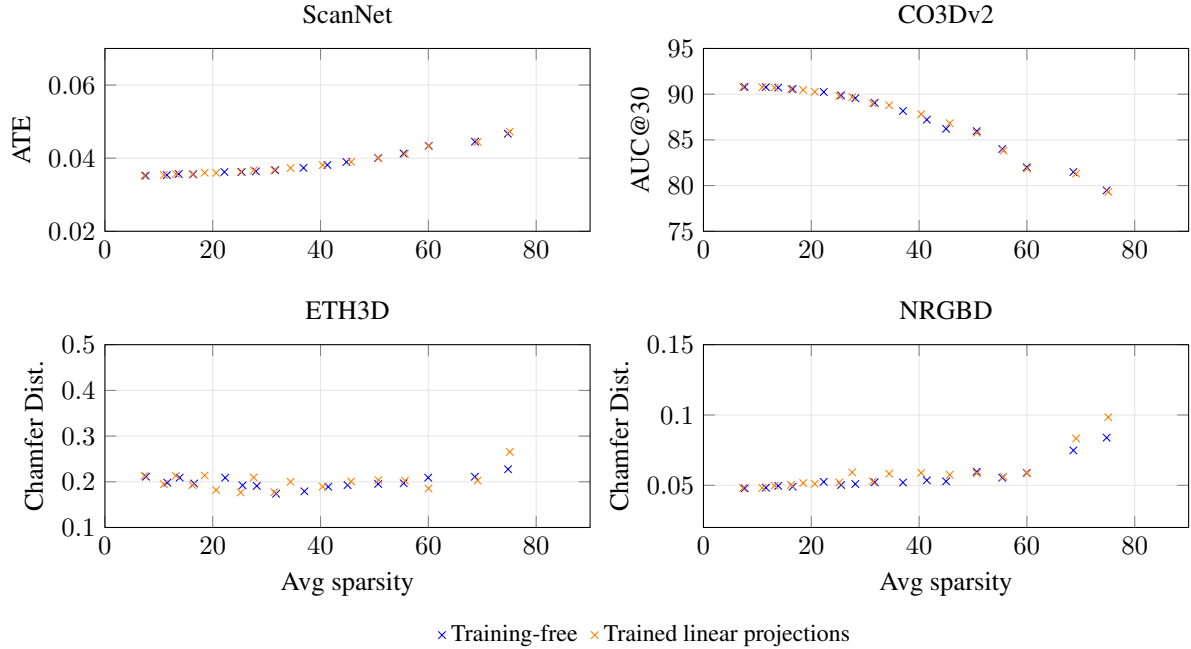


Figure A-2. **Ablation on learned linear projections.** We compare the downstream performance of training-free block-sparse mask prediction with an approach following SeerAttention [13], that is, training linear projections on top of pooled query and key features. The model with additional trained linear layers does not show significantly improved performance or robustness against increased sparsity compared to the training-free variant.

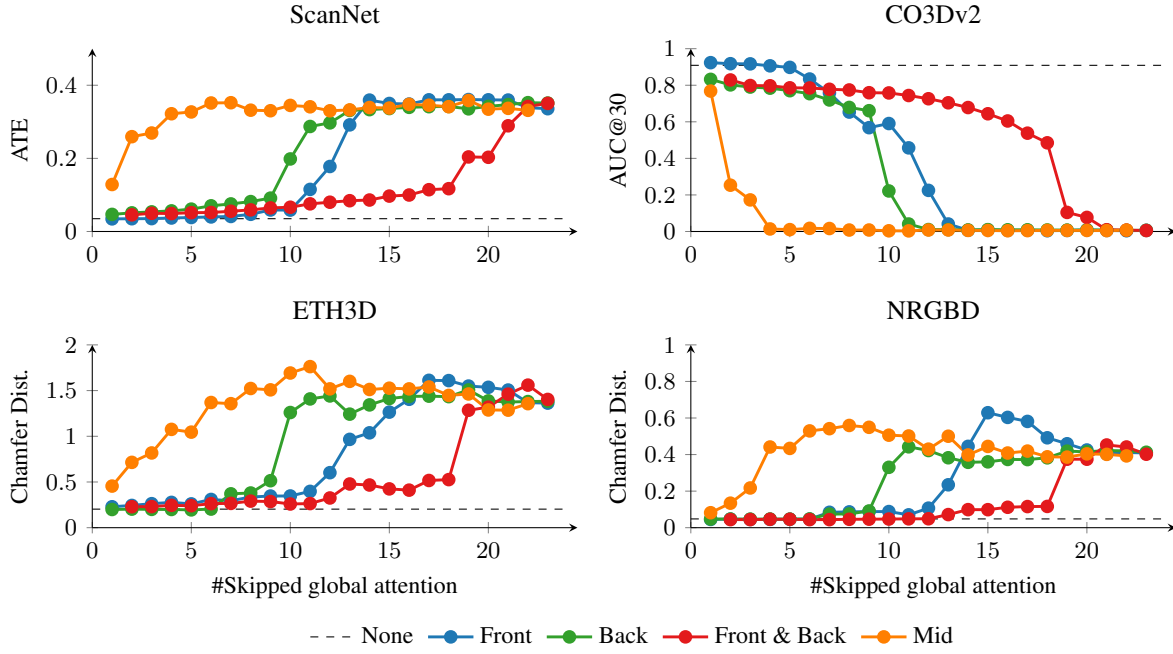


Figure A-3. **Influence of dropping global attention layers.** We skip the computation of different global attention layers in the aggregator starting with the earliest (Front), last (Back), alternating (Front & Back), or from the middle layers (Middle), and evaluate pose estimation on CO3Dv2 [23]. The x-axis denotes the total number of skipped layers. The experiment shows that the model is especially sensitive to pruning of the center layers, and robust against pruning the early and late layers.

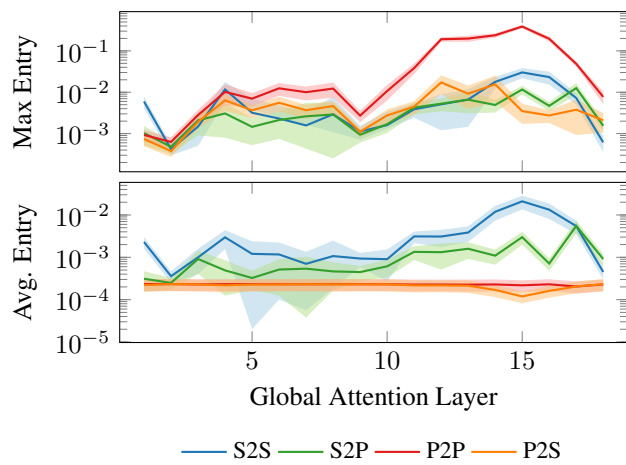


Figure A-4. **Average & maximum attention scores in π^3 's global attention maps.** Since π^3 started training from a VGGT checkpoint, the statistics are highly similar to VGGT.

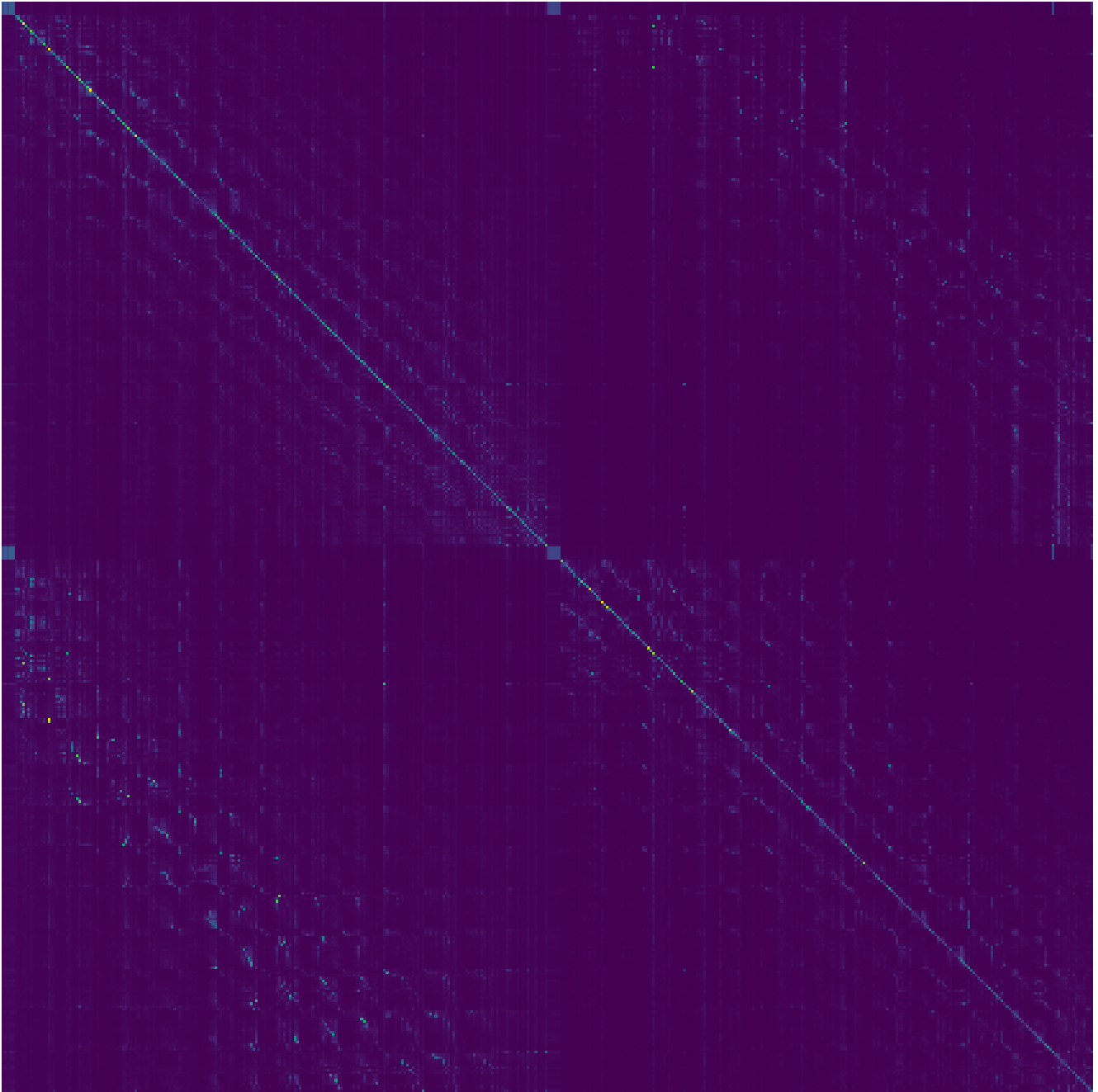


Figure A-5. Larger visualization of the global attention matrix of aggregator layer 15 of VGGT. We show the average over all heads after the softmax.

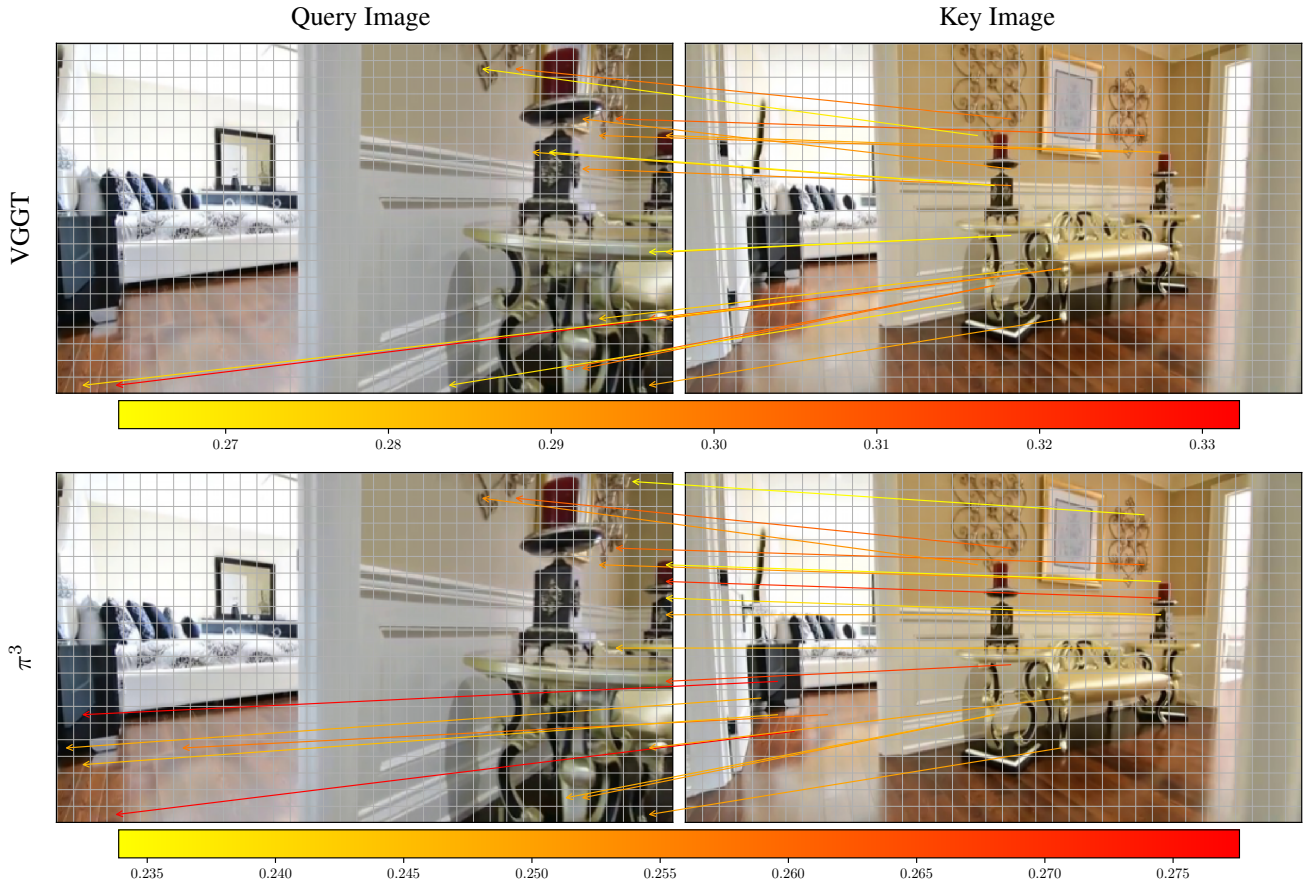


Figure A-6. Visualization of layer-15 correspondences for VGGT (top) and π^3 (bottom). Each row depicts a query image (left) and a key image (right), with arrows indicating matched points across views, where warmer colors indicates a higher attention value for the matches. Two visually identical Candles are present in both images. In both methods, the correspondences associated with one Candle in the key image are consistently mapped to the same Candle in the query image, rather than being confused with the second instance. This demonstrates the ability of the models to resolve ambiguities in scenes containing repeated objects and to maintain consistent correspondences across viewpoint changes.

Model	Acc	Comp	N.C.	Top- k (%)	CDF	Sparsity
VGGT	0.050	0.062	0.750	10	0.970	7.560
VGGT	0.053	0.062	0.746	30	0.970	11.490
VGGT	0.052	0.061	0.746	50	0.970	13.690
VGGT	0.053	0.062	0.749	40	0.950	16.390
VGGT	0.057	0.063	0.747	60	0.930	22.170
VGGT	0.054	0.061	0.747	50	0.900	25.370
VGGT	0.052	0.059	0.748	50	0.880	28.010
VGGT	0.050	0.055	0.749	50	0.850	31.600
VGGT	0.050	0.055	0.749	50	0.800	36.840
VGGT	0.053	0.058	0.747	50	0.750	41.270
VGGT	0.053	0.057	0.747	50	0.700	44.810
VGGT	0.050	0.059	0.747	70	0.700	50.670
VGGT	0.046	0.055	0.749	60	0.600	55.400
VGGT	0.050	0.059	0.746	60	0.400	60.080
VGGT	0.053	0.073	0.740	80	0.500	68.650
VGGT	0.064	0.084	0.729	80	0.400	74.740
π^3	0.055	0.073	0.743	10	0.970	8.630
π^3	0.056	0.074	0.740	30	0.970	13.370
π^3	0.051	0.066	0.746	50	0.970	15.730
π^3	0.052	0.067	0.745	40	0.950	19.000
π^3	0.058	0.076	0.741	60	0.930	25.320
π^3	0.052	0.067	0.743	50	0.900	28.980
π^3	0.052	0.066	0.743	50	0.880	31.840
π^3	0.053	0.066	0.742	50	0.850	35.630
π^3	0.055	0.066	0.741	50	0.800	40.840
π^3	0.056	0.064	0.740	50	0.750	44.710
π^3	0.058	0.064	0.736	50	0.700	47.280
π^3	0.077	0.086	0.720	70	0.700	55.440
π^3	0.070	0.074	0.723	60	0.600	57.820
π^3	0.074	0.075	0.716	60	0.400	60.080
π^3	0.083	0.084	0.709	80	0.500	72.460
π^3	0.090	0.085	0.701	80	0.400	77.100

Table A-1. Full results for Seven Scenes [28]

Model	RRA@30	RTA@30	AUC@30	Top- k (%)	CDF	Sparsity
VGGT	0.975	0.916	0.908	10	0.970	7.560
VGGT	0.975	0.915	0.908	30	0.970	11.430
VGGT	0.975	0.915	0.907	50	0.970	13.730
VGGT	0.973	0.914	0.906	40	0.950	16.430
VGGT	0.971	0.912	0.902	60	0.930	22.160
VGGT	0.967	0.910	0.899	50	0.900	25.420
VGGT	0.964	0.909	0.896	50	0.880	28.000
VGGT	0.959	0.906	0.891	50	0.850	31.600
VGGT	0.950	0.900	0.882	50	0.800	36.840
VGGT	0.941	0.895	0.872	50	0.750	41.350
VGGT	0.932	0.888	0.862	50	0.700	44.890
VGGT	0.932	0.886	0.860	70	0.700	50.810
VGGT	0.914	0.874	0.840	60	0.600	55.400
VGGT	0.896	0.862	0.820	60	0.400	60.080
VGGT	0.894	0.857	0.815	80	0.500	68.650
VGGT	0.876	0.844	0.795	80	0.400	74.740
π^3	0.976	0.917	0.910	10	0.970	8.650
π^3	0.976	0.917	0.910	30	0.970	13.510
π^3	0.976	0.916	0.909	50	0.970	16.040
π^3	0.975	0.915	0.908	40	0.950	19.130
π^3	0.974	0.913	0.905	60	0.930	25.500
π^3	0.971	0.911	0.902	50	0.900	29.030
π^3	0.969	0.909	0.899	50	0.880	31.830
π^3	0.965	0.907	0.895	50	0.850	35.570
π^3	0.959	0.902	0.888	50	0.800	40.750
π^3	0.953	0.899	0.881	50	0.750	44.680
π^3	0.946	0.895	0.875	50	0.700	47.350
π^3	0.943	0.888	0.867	70	0.700	55.120
π^3	0.928	0.883	0.855	60	0.600	57.650
π^3	0.915	0.876	0.842	60	0.400	59.950
π^3	0.906	0.861	0.825	80	0.500	72.190
π^3	0.887	0.849	0.805	80	0.400	77.030

Table A-2. Full results for Co3Dv2 [23]

Model	Acc	Comp	N.C.	Top- k (%)	CDF	Sparsity
VGGT	1.196	1.912	0.679	10	0.970	7.560
VGGT	1.198	1.901	0.678	30	0.970	11.490
VGGT	1.200	1.905	0.678	50	0.970	13.690
VGGT	1.205	1.915	0.677	40	0.950	16.390
VGGT	1.215	1.874	0.675	60	0.930	22.170
VGGT	1.226	1.894	0.674	50	0.900	25.370
VGGT	1.234	1.870	0.673	50	0.880	28.010
VGGT	1.250	1.848	0.671	50	0.850	31.600
VGGT	1.283	1.846	0.669	50	0.800	36.840
VGGT	1.319	1.864	0.668	50	0.750	41.270
VGGT	1.361	1.867	0.667	50	0.700	44.810
VGGT	1.364	1.786	0.664	70	0.700	50.670
VGGT	1.468	1.782	0.663	60	0.600	55.400
VGGT	1.573	1.767	0.660	60	0.400	60.080
VGGT	1.605	1.679	0.659	80	0.500	68.650
VGGT	1.770	1.660	0.659	80	0.400	74.740
π^3	1.864	1.812	0.648	10	0.970	8.630
π^3	1.862	1.818	0.647	30	0.970	13.370
π^3	1.865	1.820	0.647	50	0.970	15.730
π^3	1.865	1.825	0.646	40	0.950	19.000
π^3	1.878	1.822	0.648	60	0.930	25.320
π^3	1.889	1.814	0.648	50	0.900	28.980
π^3	1.900	1.815	0.649	50	0.880	31.840
π^3	1.925	1.806	0.649	50	0.850	35.630
π^3	1.979	1.799	0.651	50	0.800	40.840
π^3	2.056	1.790	0.652	50	0.750	44.710
π^3	2.167	1.792	0.654	50	0.700	47.280
π^3	2.209	1.764	0.655	70	0.700	55.440
π^3	2.506	1.843	0.657	60	0.600	57.820
π^3	3.029	1.972	0.660	60	0.400	60.080
π^3	3.068	1.940	0.660	80	0.500	72.460
π^3	3.444	2.050	0.662	80	0.400	77.100

Table A-3. Full results for DTU [16]

Model	Acc	Comp	N.C.	Top- k (%)	CDF	Sparsity
VGGT	0.232	0.190	0.886	10	0.970	7.560
VGGT	0.220	0.176	0.888	30	0.970	11.490
VGGT	0.238	0.180	0.884	50	0.970	13.690
VGGT	0.218	0.174	0.887	40	0.950	16.390
VGGT	0.231	0.187	0.874	60	0.930	22.170
VGGT	0.212	0.172	0.885	50	0.900	25.370
VGGT	0.213	0.169	0.884	50	0.880	28.010
VGGT	0.195	0.153	0.886	50	0.850	31.600
VGGT	0.201	0.158	0.880	50	0.800	36.840
VGGT	0.208	0.170	0.877	50	0.750	41.270
VGGT	0.212	0.173	0.869	50	0.700	44.810
VGGT	0.207	0.183	0.863	70	0.700	50.670
VGGT	0.217	0.177	0.863	60	0.600	55.400
VGGT	0.233	0.185	0.856	60	0.400	60.080
VGGT	0.234	0.188	0.842	80	0.500	68.650
VGGT	0.250	0.205	0.837	80	0.400	74.740
π^3	0.107	0.085	0.898	10	0.970	8.630
π^3	0.113	0.089	0.897	30	0.970	13.370
π^3	0.115	0.091	0.898	50	0.970	15.730
π^3	0.115	0.089	0.892	40	0.950	19.000
π^3	0.135	0.104	0.882	60	0.930	25.320
π^3	0.135	0.101	0.880	50	0.900	28.980
π^3	0.138	0.103	0.878	50	0.880	31.840
π^3	0.146	0.108	0.876	50	0.850	35.630
π^3	0.159	0.114	0.866	50	0.800	40.840
π^3	0.170	0.117	0.860	50	0.750	44.710
π^3	0.189	0.126	0.856	50	0.700	47.280
π^3	0.209	0.146	0.850	70	0.700	55.440
π^3	0.230	0.145	0.841	60	0.600	57.820
π^3	0.274	0.170	0.832	60	0.400	60.080
π^3	0.320	0.194	0.823	80	0.500	72.460
π^3	0.386	0.222	0.800	80	0.400	77.100

Table A-4. Full results for ETH3D [26]

Model	Acc	Comp	N.C.	Top- k (%)	CDF	Sparsity
VGGT	0.047	0.049	0.897	10	0.970	7.560
VGGT	0.047	0.049	0.899	30	0.970	11.490
VGGT	0.049	0.051	0.899	50	0.970	13.690
VGGT	0.048	0.050	0.898	40	0.950	16.390
VGGT	0.051	0.054	0.893	60	0.930	22.170
VGGT	0.049	0.051	0.897	50	0.900	25.370
VGGT	0.050	0.052	0.894	50	0.880	28.010
VGGT	0.051	0.053	0.892	50	0.850	31.600
VGGT	0.051	0.053	0.890	50	0.800	36.840
VGGT	0.053	0.054	0.885	50	0.750	41.270
VGGT	0.053	0.053	0.881	50	0.700	44.810
VGGT	0.058	0.061	0.875	70	0.700	50.670
VGGT	0.054	0.056	0.885	60	0.600	55.400
VGGT	0.057	0.060	0.875	60	0.400	60.080
VGGT	0.072	0.078	0.860	80	0.500	68.650
VGGT	0.078	0.090	0.849	80	0.400	74.740
π^3	0.028	0.028	0.907	10	0.970	8.630
π^3	0.029	0.029	0.904	30	0.970	13.370
π^3	0.030	0.030	0.902	50	0.970	15.730
π^3	0.032	0.031	0.897	40	0.950	19.000
π^3	0.033	0.032	0.898	60	0.930	25.320
π^3	0.032	0.032	0.897	50	0.900	28.980
π^3	0.033	0.032	0.896	50	0.880	31.840
π^3	0.035	0.033	0.892	50	0.850	35.630
π^3	0.039	0.036	0.884	50	0.800	40.840
π^3	0.043	0.040	0.877	50	0.750	44.710
π^3	0.048	0.043	0.868	50	0.700	47.280
π^3	0.051	0.047	0.878	70	0.700	55.440
π^3	0.058	0.049	0.862	60	0.600	57.820
π^3	0.069	0.055	0.842	60	0.400	60.080
π^3	0.074	0.063	0.835	80	0.500	72.460
π^3	0.083	0.067	0.815	80	0.400	77.100

Table A-5. Full results for NRGBD [1]

Model	RRA@30	RTA@30	AUC@30	Top- k (%)	CDF	Sparsity
VGGT	0.977	0.763	0.760	10	0.970	7.560
VGGT	0.977	0.762	0.759	30	0.970	11.430
VGGT	0.976	0.762	0.759	50	0.970	13.730
VGGT	0.976	0.759	0.756	40	0.950	16.430
VGGT	0.975	0.754	0.751	60	0.930	22.160
VGGT	0.976	0.752	0.749	50	0.900	25.420
VGGT	0.975	0.750	0.746	50	0.880	28.000
VGGT	0.975	0.745	0.742	50	0.850	31.600
VGGT	0.975	0.738	0.735	50	0.800	36.840
VGGT	0.974	0.732	0.729	50	0.750	41.350
VGGT	0.974	0.726	0.723	50	0.700	44.890
VGGT	0.972	0.721	0.718	70	0.700	50.810
VGGT	0.972	0.712	0.709	60	0.600	55.400
VGGT	0.971	0.699	0.696	60	0.400	60.080
VGGT	0.967	0.687	0.683	80	0.500	68.650
VGGT	0.965	0.675	0.671	80	0.400	74.740
π^3	0.992	0.871	0.870	10	0.970	8.650
π^3	0.992	0.868	0.867	30	0.970	13.510
π^3	0.992	0.866	0.865	50	0.970	16.040
π^3	0.992	0.861	0.860	40	0.950	19.130
π^3	0.992	0.854	0.853	60	0.930	25.500
π^3	0.992	0.847	0.846	50	0.900	29.030
π^3	0.992	0.841	0.840	50	0.880	31.830
π^3	0.991	0.833	0.832	50	0.850	35.570
π^3	0.991	0.821	0.820	50	0.800	40.750
π^3	0.991	0.812	0.810	50	0.750	44.680
π^3	0.990	0.805	0.804	50	0.700	47.350
π^3	0.990	0.798	0.796	70	0.700	55.120
π^3	0.989	0.784	0.783	60	0.600	57.650
π^3	0.988	0.776	0.774	60	0.400	59.950
π^3	0.986	0.762	0.760	80	0.500	72.190
π^3	0.984	0.747	0.745	80	0.400	77.030

Table A-6. Full results for Real Estate 10K [41]

Model	ATE	RPEtrans	RPErot	Top- k (%)	CDF	Sparsity
VGGT	0.035	0.015	0.382	10	0.970	7.560
VGGT	0.035	0.015	0.382	30	0.970	11.490
VGGT	0.036	0.016	0.393	50	0.970	13.690
VGGT	0.036	0.015	0.384	40	0.950	16.390
VGGT	0.036	0.016	0.387	60	0.930	22.170
VGGT	0.036	0.016	0.389	50	0.900	25.370
VGGT	0.036	0.016	0.392	50	0.880	28.010
VGGT	0.037	0.016	0.395	50	0.850	31.600
VGGT	0.037	0.016	0.402	50	0.800	36.840
VGGT	0.038	0.017	0.410	50	0.750	41.270
VGGT	0.039	0.017	0.421	50	0.700	44.810
VGGT	0.040	0.017	0.428	70	0.700	50.670
VGGT	0.041	0.018	0.451	60	0.600	55.400
VGGT	0.043	0.019	0.481	60	0.400	60.080
VGGT	0.044	0.019	0.484	80	0.500	68.650
VGGT	0.047	0.020	0.527	80	0.400	74.740
π^3	0.031	0.013	0.345	10	0.970	8.630
π^3	0.031	0.013	0.345	30	0.970	13.370
π^3	0.030	0.013	0.346	50	0.970	15.730
π^3	0.031	0.013	0.346	40	0.950	19.000
π^3	0.031	0.013	0.348	60	0.930	25.320
π^3	0.031	0.013	0.349	50	0.900	28.980
π^3	0.031	0.013	0.351	50	0.880	31.840
π^3	0.031	0.013	0.353	50	0.850	35.630
π^3	0.032	0.013	0.356	50	0.800	40.840
π^3	0.032	0.013	0.359	50	0.750	44.710
π^3	0.032	0.014	0.363	50	0.700	47.280
π^3	0.033	0.014	0.369	70	0.700	55.440
π^3	0.033	0.014	0.375	60	0.600	57.820
π^3	0.034	0.014	0.382	60	0.400	60.080
π^3	0.035	0.015	0.397	80	0.500	72.460
π^3	0.037	0.015	0.418	80	0.400	77.100

Table A-7. Full results for ScanNet [6].

Model	ATE	RPEtrans	RPErot	Top- k (%)	CDF	Sparsity
VGGT	0.012	0.010	0.352	10	0.970	7.560
VGGT	0.012	0.010	0.352	30	0.970	11.490
VGGT	0.012	0.010	0.353	50	0.970	13.690
VGGT	0.012	0.010	0.354	40	0.950	16.390
VGGT	0.013	0.011	0.356	60	0.930	22.170
VGGT	0.013	0.011	0.358	50	0.900	25.370
VGGT	0.013	0.011	0.359	50	0.880	28.010
VGGT	0.014	0.011	0.361	50	0.850	31.600
VGGT	0.014	0.012	0.366	50	0.800	36.840
VGGT	0.015	0.012	0.370	50	0.750	41.270
VGGT	0.016	0.013	0.376	50	0.700	44.810
VGGT	0.017	0.013	0.379	70	0.700	50.670
VGGT	0.018	0.014	0.390	60	0.600	55.400
VGGT	0.020	0.015	0.414	60	0.400	60.080
VGGT	0.020	0.015	0.410	80	0.500	68.650
VGGT	0.024	0.016	0.453	80	0.400	74.740
π^3	0.014	0.009	0.349	10	0.970	8.630
π^3	0.014	0.009	0.350	30	0.970	13.370
π^3	0.014	0.009	0.350	50	0.970	15.730
π^3	0.014	0.009	0.351	40	0.950	19.000
π^3	0.014	0.009	0.353	60	0.930	25.320
π^3	0.015	0.010	0.354	50	0.900	28.980
π^3	0.015	0.010	0.355	50	0.880	31.840
π^3	0.015	0.010	0.357	50	0.850	35.630
π^3	0.016	0.011	0.360	50	0.800	40.840
π^3	0.017	0.011	0.361	50	0.750	44.710
π^3	0.017	0.011	0.363	50	0.700	47.280
π^3	0.019	0.012	0.371	70	0.700	55.440
π^3	0.019	0.012	0.373	60	0.600	57.820
π^3	0.020	0.013	0.375	60	0.400	60.080
π^3	0.022	0.014	0.387	80	0.500	72.460
π^3	0.023	0.014	0.401	80	0.400	77.100

Table A-8. Full results for TUM [29].

Model	RRA@5	RRA@15	RRA@30	RTA@5	RTA@15	RTA@30	AUC@5	AUC@15	AUC@30	ATE	Top- <i>k</i> (%)	CDF	Sparsity
VGGT	0.836	0.897	0.914	0.812	0.882	0.909	0.757	0.849	0.878	0.033	10	0.970	7.560
VGGT	0.837	0.897	0.914	0.809	0.882	0.910	0.755	0.848	0.878	0.033	30	0.970	11.490
VGGT	0.827	0.895	0.914	0.802	0.878	0.908	0.745	0.844	0.877	0.032	40	0.950	16.390
VGGT	0.731	0.857	0.891	0.736	0.852	0.893	0.639	0.804	0.852	0.035	50	0.700	44.810
VGGT	0.774	0.871	0.898	0.768	0.864	0.899	0.688	0.821	0.862	0.033	50	0.800	36.840
VGGT	0.814	0.885	0.907	0.795	0.874	0.905	0.732	0.837	0.871	0.032	50	0.900	25.370
VGGT	0.751	0.863	0.894	0.753	0.858	0.897	0.663	0.812	0.857	0.034	50	0.750	41.270
VGGT	0.796	0.879	0.902	0.783	0.870	0.902	0.710	0.829	0.866	0.033	50	0.850	31.600
VGGT	0.807	0.882	0.905	0.791	0.873	0.904	0.723	0.834	0.869	0.032	50	0.880	28.010
VGGT	0.838	0.896	0.915	0.806	0.881	0.911	0.753	0.847	0.878	0.032	50	0.970	13.690
VGGT	0.631	0.825	0.876	0.658	0.823	0.879	0.527	0.762	0.831	0.035	60	0.400	60.080
VGGT	0.678	0.841	0.884	0.695	0.838	0.887	0.580	0.782	0.842	0.035	60	0.600	55.400
VGGT	0.823	0.890	0.911	0.795	0.875	0.905	0.738	0.840	0.873	0.033	60	0.930	22.170
VGGT	0.723	0.857	0.892	0.723	0.848	0.892	0.623	0.798	0.849	0.035	70	0.700	50.670
VGGT	0.569	0.800	0.865	0.607	0.801	0.866	0.463	0.734	0.817	0.037	80	0.400	74.740
VGGT	0.602	0.813	0.870	0.636	0.813	0.873	0.501	0.750	0.825	0.037	80	0.500	68.650
π^3	0.842	0.908	0.929	0.836	0.905	0.931	0.780	0.872	0.903	0.020	10	0.970	8.630
π^3	0.844	0.908	0.927	0.837	0.904	0.931	0.781	0.873	0.903	0.020	30	0.970	13.370
π^3	0.839	0.906	0.926	0.831	0.902	0.930	0.775	0.871	0.902	0.020	40	0.950	19.000
π^3	0.753	0.871	0.908	0.779	0.884	0.920	0.680	0.833	0.882	0.019	50	0.700	47.280
π^3	0.788	0.884	0.915	0.801	0.892	0.924	0.717	0.848	0.890	0.019	50	0.800	40.840
π^3	0.826	0.899	0.923	0.821	0.899	0.928	0.758	0.863	0.897	0.019	50	0.900	28.980
π^3	0.766	0.876	0.911	0.789	0.887	0.922	0.694	0.838	0.885	0.019	50	0.750	44.710
π^3	0.808	0.892	0.919	0.813	0.896	0.926	0.739	0.856	0.894	0.019	50	0.850	35.630
π^3	0.819	0.896	0.921	0.818	0.898	0.927	0.750	0.860	0.896	0.019	50	0.880	31.840
π^3	0.844	0.908	0.928	0.835	0.904	0.931	0.780	0.873	0.903	0.019	50	0.970	15.730
π^3	0.679	0.845	0.894	0.731	0.866	0.911	0.603	0.804	0.867	0.020	60	0.400	60.080
π^3	0.702	0.853	0.897	0.748	0.872	0.914	0.627	0.813	0.871	0.019	60	0.600	57.820
π^3	0.836	0.905	0.925	0.826	0.900	0.928	0.769	0.868	0.900	0.019	60	0.930	25.320
π^3	0.734	0.866	0.903	0.767	0.878	0.917	0.659	0.826	0.876	0.020	70	0.700	55.440
π^3	0.570	0.797	0.865	0.656	0.831	0.890	0.492	0.752	0.835	0.025	80	0.400	77.100
π^3	0.619	0.819	0.877	0.686	0.843	0.897	0.539	0.773	0.847	0.024	80	0.500	72.460

Table A-9. Full results for Tanks & Temples [17] (25 frames).

Model	RRA@5	RRA@15	RRA@30	RTA@5	RTA@15	RTA@30	AUC@5	AUC@15	AUC@30	ATE	Top- <i>k</i> (%)	CDF	Sparsity
VGGT	0.842	0.896	0.913	0.811	0.882	0.910	0.763	0.850	0.879	0.023	10	0.970	7.560
VGGT	0.840	0.895	0.913	0.811	0.882	0.909	0.762	0.850	0.879	0.023	30	0.970	11.490
VGGT	0.835	0.894	0.912	0.807	0.881	0.909	0.755	0.848	0.878	0.023	40	0.950	16.390
VGGT	0.729	0.857	0.894	0.734	0.852	0.894	0.635	0.804	0.855	0.024	50	0.700	44.810
VGGT	0.775	0.873	0.901	0.768	0.866	0.901	0.686	0.823	0.865	0.024	50	0.800	36.840
VGGT	0.816	0.887	0.908	0.795	0.876	0.906	0.734	0.840	0.873	0.023	50	0.900	25.370
VGGT	0.750	0.865	0.897	0.752	0.859	0.897	0.661	0.813	0.860	0.024	50	0.750	41.270
VGGT	0.796	0.880	0.905	0.782	0.871	0.904	0.711	0.832	0.869	0.023	50	0.850	31.600
VGGT	0.808	0.884	0.907	0.791	0.874	0.905	0.725	0.837	0.872	0.023	50	0.880	28.010
VGGT	0.838	0.895	0.912	0.810	0.882	0.910	0.759	0.850	0.879	0.023	50	0.970	13.690
VGGT	0.624	0.820	0.874	0.653	0.820	0.876	0.521	0.760	0.831	0.025	60	0.400	60.080
VGGT	0.676	0.839	0.885	0.696	0.838	0.886	0.580	0.783	0.844	0.024	60	0.600	55.400
VGGT	0.824	0.889	0.910	0.801	0.878	0.908	0.743	0.843	0.875	0.023	60	0.930	22.170
VGGT	0.720	0.855	0.892	0.729	0.851	0.893	0.628	0.802	0.854	0.023	70	0.700	50.670
VGGT	0.573	0.799	0.863	0.610	0.803	0.868	0.470	0.736	0.818	0.025	80	0.400	74.740
VGGT	0.612	0.813	0.870	0.642	0.815	0.873	0.511	0.753	0.826	0.025	80	0.500	68.650
π^3	0.850	0.907	0.926	0.843	0.904	0.928	0.795	0.874	0.902	0.015	10	0.970	8.630
π^3	0.847	0.906	0.926	0.841	0.904	0.928	0.792	0.873	0.902	0.015	30	0.970	13.370
π^3	0.842	0.903	0.925	0.838	0.902	0.927	0.786	0.871	0.901	0.015	40	0.950	19.000
π^3	0.750	0.869	0.906	0.785	0.883	0.918	0.683	0.834	0.881	0.016	50	0.700	47.280
π^3	0.783	0.881	0.912	0.807	0.891	0.921	0.720	0.848	0.888	0.016	50	0.800	40.840
π^3	0.823	0.896	0.920	0.829	0.899	0.926	0.765	0.863	0.896	0.015	50	0.900	28.980
π^3	0.765	0.874	0.909	0.795	0.887	0.920	0.699	0.840	0.884	0.016	50	0.750	44.710
π^3	0.804	0.889	0.916	0.819	0.896	0.924	0.744	0.856	0.892	0.015	50	0.850	35.630
π^3	0.816	0.893	0.918	0.825	0.898	0.925	0.757	0.861	0.895	0.015	50	0.880	31.840
π^3	0.845	0.905	0.926	0.839	0.903	0.928	0.789	0.872	0.902	0.015	50	0.970	15.730
π^3	0.680	0.841	0.891	0.738	0.866	0.909	0.607	0.805	0.866	0.016	60	0.400	60.080
π^3	0.704	0.851	0.897	0.754	0.872	0.912	0.632	0.815	0.871	0.016	60	0.600	57.820
π^3	0.832	0.901	0.924	0.832	0.900	0.927	0.774	0.867	0.899	0.015	60	0.930	25.320
π^3	0.734	0.864	0.904	0.774	0.879	0.916	0.664	0.827	0.878	0.016	70	0.700	55.440
π^3	0.579	0.803	0.872	0.670	0.842	0.897	0.502	0.764	0.846	0.016	80	0.400	77.100
π^3	0.629	0.823	0.882	0.703	0.854	0.904	0.553	0.784	0.857	0.016	80	0.500	72.460

Table A-10. Full results for Tanks & Temples [17] (50 frames).

Model	RRA@5	RRA@15	RRA@30	RTA@5	RTA@15	RTA@30	AUC@5	AUC@15	AUC@30	ATE	Top- k (%)	CDF	Sparsity
VGGT	0.842	0.897	0.913	0.811	0.883	0.911	0.760	0.850	0.880	0.015	10	0.970	7.560
VGGT	0.841	0.896	0.913	0.810	0.882	0.911	0.759	0.850	0.879	0.015	30	0.970	11.490
VGGT	0.835	0.894	0.912	0.807	0.881	0.911	0.752	0.847	0.878	0.016	40	0.950	16.390
VGGT	0.730	0.859	0.894	0.739	0.856	0.897	0.638	0.807	0.857	0.016	50	0.700	44.810
VGGT	0.774	0.874	0.902	0.770	0.868	0.904	0.687	0.825	0.867	0.016	50	0.800	36.840
VGGT	0.817	0.888	0.909	0.797	0.878	0.909	0.733	0.841	0.875	0.016	50	0.900	25.370
VGGT	0.752	0.867	0.898	0.755	0.862	0.901	0.662	0.816	0.862	0.016	50	0.750	41.270
VGGT	0.796	0.882	0.906	0.785	0.873	0.906	0.711	0.833	0.871	0.016	50	0.850	31.600
VGGT	0.809	0.886	0.908	0.793	0.876	0.908	0.724	0.838	0.873	0.016	50	0.880	28.010
VGGT	0.840	0.896	0.913	0.809	0.882	0.911	0.757	0.849	0.879	0.016	50	0.970	13.690
VGGT	0.627	0.821	0.874	0.655	0.821	0.878	0.522	0.760	0.831	0.017	60	0.400	60.080
VGGT	0.681	0.841	0.884	0.700	0.839	0.888	0.583	0.785	0.845	0.017	60	0.600	55.400
VGGT	0.827	0.892	0.911	0.802	0.880	0.910	0.743	0.844	0.877	0.016	60	0.930	22.170
VGGT	0.723	0.856	0.892	0.730	0.851	0.895	0.629	0.802	0.855	0.017	70	0.700	50.670
VGGT	0.581	0.802	0.864	0.615	0.803	0.867	0.474	0.737	0.819	0.017	80	0.400	74.740
VGGT	0.624	0.818	0.872	0.650	0.817	0.875	0.520	0.757	0.830	0.017	80	0.500	68.650
π^3	0.853	0.909	0.926	0.844	0.905	0.928	0.795	0.875	0.902	0.012	10	0.970	8.630
π^3	0.851	0.908	0.926	0.843	0.904	0.928	0.793	0.874	0.902	0.012	30	0.970	13.370
π^3	0.846	0.906	0.925	0.840	0.903	0.928	0.787	0.872	0.901	0.012	40	0.950	19.000
π^3	0.758	0.876	0.910	0.785	0.883	0.918	0.684	0.836	0.883	0.012	50	0.700	47.280
π^3	0.792	0.888	0.916	0.806	0.891	0.921	0.721	0.849	0.889	0.012	50	0.800	40.840
π^3	0.830	0.901	0.922	0.830	0.899	0.926	0.767	0.865	0.897	0.012	50	0.900	28.980
π^3	0.773	0.882	0.913	0.795	0.887	0.919	0.700	0.842	0.886	0.012	50	0.750	44.710
π^3	0.812	0.895	0.919	0.818	0.895	0.924	0.745	0.858	0.894	0.012	50	0.850	35.630
π^3	0.824	0.898	0.921	0.825	0.898	0.925	0.758	0.862	0.896	0.012	50	0.880	31.840
π^3	0.850	0.907	0.925	0.842	0.904	0.928	0.792	0.874	0.902	0.012	50	0.970	15.730
π^3	0.686	0.852	0.897	0.740	0.867	0.909	0.609	0.809	0.870	0.012	60	0.400	60.080
π^3	0.709	0.860	0.901	0.755	0.872	0.912	0.633	0.818	0.874	0.012	60	0.600	57.820
π^3	0.840	0.904	0.924	0.834	0.901	0.927	0.778	0.869	0.899	0.012	60	0.930	25.320
π^3	0.743	0.871	0.907	0.774	0.879	0.916	0.666	0.830	0.879	0.012	70	0.700	55.440
π^3	0.589	0.814	0.878	0.672	0.841	0.897	0.508	0.770	0.849	0.012	80	0.400	77.100
π^3	0.640	0.833	0.888	0.705	0.854	0.903	0.558	0.790	0.859	0.012	80	0.500	72.460

Table A-11. Full results for Tanks & Temples [17] (100 frames).

Model	RRA@5	RRA@15	RRA@30	RTA@5	RTA@15	RTA@30	AUC@5	AUC@15	AUC@30	ATE	Top- <i>k</i> (%)	CDF	Sparsity
VGGT	0.833	0.890	0.909	0.797	0.875	0.906	0.746	0.840	0.873	0.011	10	0.970	7.560
VGGT	0.832	0.891	0.909	0.797	0.875	0.906	0.745	0.840	0.873	0.011	30	0.970	11.490
VGGT	0.826	0.889	0.908	0.794	0.874	0.906	0.738	0.838	0.872	0.011	40	0.950	16.390
VGGT	0.717	0.851	0.888	0.725	0.847	0.890	0.622	0.794	0.848	0.012	50	0.700	44.810
VGGT	0.764	0.867	0.897	0.757	0.860	0.898	0.672	0.814	0.859	0.011	50	0.800	36.840
VGGT	0.807	0.883	0.905	0.784	0.870	0.904	0.719	0.831	0.868	0.011	50	0.900	25.370
VGGT	0.741	0.859	0.893	0.741	0.853	0.894	0.646	0.804	0.853	0.012	50	0.750	41.270
VGGT	0.786	0.875	0.901	0.772	0.865	0.901	0.696	0.823	0.863	0.011	50	0.850	31.600
VGGT	0.799	0.879	0.903	0.780	0.868	0.903	0.710	0.828	0.866	0.011	50	0.880	28.010
VGGT	0.831	0.890	0.909	0.796	0.875	0.906	0.743	0.840	0.873	0.011	50	0.970	13.690
VGGT	0.614	0.814	0.868	0.644	0.813	0.871	0.507	0.750	0.823	0.013	60	0.400	60.080
VGGT	0.668	0.832	0.878	0.688	0.831	0.881	0.568	0.773	0.836	0.012	60	0.600	55.400
VGGT	0.817	0.885	0.906	0.788	0.872	0.904	0.728	0.834	0.870	0.011	60	0.930	22.170
VGGT	0.711	0.848	0.886	0.719	0.844	0.889	0.614	0.791	0.846	0.012	70	0.700	50.670
VGGT	0.571	0.797	0.860	0.608	0.797	0.862	0.462	0.729	0.812	0.013	80	0.400	74.740
VGGT	0.616	0.814	0.869	0.644	0.813	0.871	0.510	0.750	0.823	0.013	80	0.500	68.650
π^3	0.850	0.906	0.924	0.838	0.900	0.924	0.788	0.870	0.899	0.009	10	0.970	8.630
π^3	0.848	0.904	0.923	0.836	0.899	0.924	0.786	0.868	0.898	0.009	30	0.970	13.370
π^3	0.843	0.902	0.922	0.833	0.898	0.923	0.780	0.866	0.897	0.009	40	0.950	19.000
π^3	0.757	0.872	0.906	0.781	0.879	0.914	0.681	0.831	0.878	0.009	50	0.700	47.280
π^3	0.791	0.884	0.912	0.800	0.886	0.917	0.717	0.843	0.885	0.009	50	0.800	40.840
π^3	0.829	0.897	0.919	0.824	0.895	0.922	0.762	0.860	0.893	0.009	50	0.900	28.980
π^3	0.772	0.877	0.909	0.790	0.882	0.915	0.696	0.836	0.881	0.009	50	0.750	44.710
π^3	0.811	0.891	0.916	0.813	0.891	0.920	0.740	0.852	0.889	0.009	50	0.850	35.630
π^3	0.822	0.895	0.918	0.820	0.893	0.921	0.754	0.857	0.892	0.009	50	0.880	31.840
π^3	0.846	0.903	0.923	0.835	0.899	0.924	0.784	0.868	0.898	0.009	50	0.970	15.730
π^3	0.690	0.849	0.894	0.739	0.864	0.906	0.611	0.805	0.865	0.009	60	0.400	60.080
π^3	0.713	0.857	0.898	0.754	0.869	0.909	0.635	0.814	0.870	0.009	60	0.600	57.820
π^3	0.836	0.899	0.920	0.828	0.896	0.923	0.772	0.863	0.895	0.009	60	0.930	25.320
π^3	0.744	0.868	0.904	0.771	0.875	0.912	0.665	0.825	0.875	0.009	70	0.700	55.440
π^3	0.598	0.814	0.876	0.677	0.841	0.895	0.516	0.768	0.846	0.009	80	0.400	77.100
π^3	0.649	0.834	0.886	0.710	0.853	0.901	0.567	0.789	0.857	0.009	80	0.500	72.460

Table A-12. Full results for Tanks & Temples [17] (200 frames).

Model	RRA@5	RRA@15	RRA@30	RTA@5	RTA@15	RTA@30	AUC@5	AUC@15	AUC@30	ATE	Top-k (%)	CDF	Sparsity
VGGT	0.728	0.824	0.862	0.723	0.826	0.871	0.645	0.772	0.824	0.008	10	0.970	7.560
VGGT	0.729	0.823	0.861	0.723	0.826	0.871	0.645	0.771	0.823	0.009	30	0.970	11.490
VGGT	0.723	0.820	0.859	0.721	0.826	0.872	0.639	0.768	0.821	0.008	40	0.950	16.390
VGGT	0.613	0.776	0.832	0.654	0.798	0.856	0.526	0.721	0.791	0.009	50	0.700	44.810
VGGT	0.658	0.795	0.843	0.685	0.812	0.864	0.573	0.741	0.804	0.009	50	0.800	36.840
VGGT	0.703	0.813	0.854	0.711	0.822	0.870	0.619	0.760	0.816	0.008	50	0.900	25.370
VGGT	0.635	0.786	0.838	0.670	0.805	0.860	0.549	0.731	0.798	0.009	50	0.750	41.270
VGGT	0.681	0.804	0.849	0.700	0.817	0.867	0.597	0.752	0.810	0.009	50	0.850	31.600
VGGT	0.695	0.810	0.853	0.707	0.821	0.869	0.610	0.757	0.814	0.008	50	0.880	28.010
VGGT	0.727	0.821	0.860	0.722	0.826	0.872	0.643	0.769	0.821	0.009	50	0.970	13.690
VGGT	0.510	0.727	0.798	0.572	0.757	0.829	0.418	0.666	0.754	0.009	60	0.400	60.080
VGGT	0.561	0.750	0.813	0.613	0.778	0.843	0.472	0.693	0.771	0.009	60	0.600	55.400
VGGT	0.712	0.815	0.855	0.714	0.823	0.870	0.627	0.763	0.816	0.008	60	0.930	22.170
VGGT	0.599	0.767	0.824	0.643	0.794	0.853	0.512	0.712	0.783	0.009	70	0.700	50.670
VGGT	0.460	0.701	0.781	0.530	0.736	0.815	0.369	0.639	0.736	0.009	80	0.400	74.740
VGGT	0.501	0.719	0.791	0.564	0.753	0.825	0.410	0.659	0.748	0.009	80	0.500	68.650
π^3	0.753	0.823	0.849	0.756	0.834	0.866	0.689	0.786	0.824	0.006	10	0.970	8.630
π^3	0.750	0.822	0.848	0.754	0.834	0.866	0.685	0.785	0.823	0.006	30	0.970	13.370
π^3	0.745	0.820	0.847	0.751	0.832	0.866	0.680	0.783	0.822	0.006	40	0.950	19.000
π^3	0.659	0.791	0.833	0.699	0.813	0.856	0.585	0.749	0.804	0.006	50	0.700	47.280
π^3	0.691	0.803	0.838	0.719	0.820	0.860	0.618	0.762	0.811	0.006	50	0.800	40.840
π^3	0.730	0.816	0.845	0.742	0.829	0.864	0.662	0.777	0.819	0.006	50	0.900	28.980
π^3	0.674	0.796	0.835	0.707	0.816	0.857	0.599	0.755	0.807	0.006	50	0.750	44.710
π^3	0.711	0.810	0.842	0.731	0.825	0.862	0.641	0.770	0.815	0.006	50	0.850	35.630
π^3	0.723	0.813	0.844	0.738	0.828	0.863	0.654	0.775	0.817	0.006	50	0.880	31.840
π^3	0.748	0.821	0.848	0.753	0.833	0.866	0.684	0.785	0.823	0.006	50	0.970	15.730
π^3	0.595	0.768	0.821	0.659	0.799	0.849	0.518	0.725	0.792	0.006	60	0.400	60.080
π^3	0.613	0.775	0.824	0.671	0.803	0.851	0.537	0.732	0.795	0.006	60	0.600	57.820
π^3	0.738	0.818	0.846	0.747	0.831	0.865	0.672	0.781	0.820	0.006	60	0.930	25.320
π^3	0.643	0.786	0.830	0.688	0.809	0.854	0.566	0.743	0.801	0.006	70	0.700	55.440
π^3	0.500	0.732	0.802	0.591	0.774	0.837	0.421	0.686	0.772	0.006	80	0.400	77.100
π^3	0.548	0.751	0.812	0.624	0.786	0.843	0.468	0.705	0.782	0.006	80	0.500	72.460

Table A-13. Full results for Tanks & Temples [17] (full length).